

Banner appropriate to article type will appear here in typeset article

# High-Reynolds-number turbulent boundary layers under adverse pressure gradients. Part 2. A composite mean velocity profile

Ahmad Zarei, Mitchell Lozier, Rahul Deshpande and Ivan Marusic<sup>†</sup>

Department of Mechanical Engineering, The University of Melbourne, Victoria 3010, Australia

(Received xx; revised xx; accepted xx)

A robust composite mean velocity profile is developed for turbulent boundary layers (TBLs) subjected to adverse pressure gradients (APGs), extending the composite formulation for generic pressure-gradient TBLs proposed by Nickels (*J. Fluid Mech.*, vol. 521, 2004). Several modifications are introduced to capture characteristic features of APG flows. A new parameter accounts for pressure-gradient history effects in the wake region, a velocity-overshoot function is incorporated in the inner region, and the wake function is reformulated using an independent, physically motivated definition of the boundary-layer thickness. A compilation of APG TBL datasets from the literature, including the new dataset presented in Part 1, is used to assess and refine the formulation. The resulting composite profile contains three physically meaningful parameters that capture pressure-gradient effects on the mean velocity profile, determined through nonlinear curve fitting. These parameters form the basis of a framework for identifying ‘well-behaved’ APG TBLs and as well as quantifying the strength of pressure-gradient history effects. The composite profile further enables reliable estimation of the friction velocity and boundary-layer thickness in well-behaved APG TBLs, providing a practical tool for scaling analyses when these quantities are not directly measurable. Its analytical form yields improved estimates of mean velocity gradients, facilitating evaluation of the indicator function and identification of inflection points. Finally, the formulation provides predictive capability for both the coefficients and spatial extent of the logarithmic region of the mean streamwise velocity profile, enabling evaluation of its universality in high-Reynolds-number APG TBLs. This reveals that the von Kármán coefficient approaches an invariant value of  $\kappa \approx 0.39$  at sufficiently high Reynolds numbers, independent of pressure-gradient effects.

## 1. Introduction

In Part 1 of this study, the influence of local and upstream pressure-gradients (PG) on high-Reynolds-number adverse-pressure-gradient (APG) turbulent boundary layers (TBLs) was examined, demonstrating that PG history can significantly modify the mean velocity profile. Building on those findings, the present paper focuses on the wall-normal structure of the mean streamwise velocity in APG TBLs and the development of a composite representation of this profile.

The mean velocity profile is of particular interest because it is directly associated with

<sup>†</sup> Email address for correspondence: imarusic@unimelb.edu.au

quantities of engineering relevance, such as the skin-friction drag generated by the TBL (Panton 2005). More broadly, a well-resolved mean velocity profile is a fundamental component in the development of mixing-length and eddy-viscosity models, which can be used to predict the Reynolds stress distribution of the TBL (Subrahmanyam *et al.* 2022). It also plays a central role in resolvent-based descriptions of wall-bounded turbulence, where the mean profile acts as the base flow that governs the amplification and organisation of coherent motions (Sharma & McKeon 2013).

These uses make accurate knowledge of the mean velocity profile valuable for both simulations and experiments, particularly when quantities such as the Reynolds stresses or the wall-shear stress cannot be measured directly. The importance of such approaches increases with the friction Reynolds number ( $Re_\tau = \delta U_\tau / \nu$ ), as numerical simulations become more expensive and experimental measurements of Reynolds stresses become increasingly difficult. Here,  $\delta$  denotes the boundary-layer thickness (determined in this manuscript using the method of Lozier *et al.* 2025),  $U_\tau$  is the friction velocity (related to the wall-shear stress through  $\tau_w = \rho U_\tau^2$ ),  $\rho$  is the density, and  $\nu$  is the kinematic viscosity.

For these reasons, the development of analytical expressions describing the mean velocity profile has been an enduring objective in wall-bounded turbulence research (Panton 2005). Such descriptions take a variety of forms (e.g. the integral formulations of Subrahmanyam *et al.* 2022; Cantwell *et al.* 2022; Yang *et al.* 2024; Shu & Xu 2025); one widely used approach is the composite formulation. In composite models, the mean profile is constructed by combining expressions that represent the dominant physics of different regions of the boundary layer (e.g. the inner, overlap, and wake regions) into a single continuous profile (see Nickels 2004). These formulations are typically expressed in terms of normalised variables, with the mean streamwise velocity  $U$  and wall-normal coordinate  $z$  written in inner units (denoted by the superscript ‘+’), scaled by the viscous velocity ( $U_\tau$ ) and length ( $\nu/U_\tau$ ) scales.

It is well known that TBL statistics, including the mean velocity profile, depend on several flow parameters such as  $Re_\tau$ , streamwise pressure gradients and surface roughness. Consequently, developing a robust and general composite representation of the mean velocity profile is challenging. Such a formulation must capture the underlying physics across the different regions of the boundary layer while remaining consistent with high-fidelity datasets spanning a broad range of flow conditions.

### 1.1. Composite mean velocity profile formulations for the TBL

We briefly review the development of composite formulations for the mean velocity profile in turbulent boundary layers. In the classical view, the composite profile follows a wall–wake structure consisting of two functional relationships commonly referred to as the ‘law of the wall’ and the ‘law of the wake’ (Coles 1956; Marusic *et al.* 2010):

$$U^+ = f(z^+) + g(\Pi, \eta), \quad (1.1)$$

where the wall function,  $f$ , depends on the viscous-scaled wall-normal distance ( $z^+ = zU_\tau/\nu$ ), while the wake function,  $g$ , depends on the outer-scaled wall-normal distance ( $\eta = z/\delta$ ) and Coles’ wake-strength parameter,  $\Pi$ .

The wall function can be further decomposed into two fundamental scaling laws obtained through a range of arguments (see Millikan 1938; Clauser 1956; Coles 1956; Panton 2005; Marusic *et al.* 2010). The first applies very near the wall ( $z^+ \lesssim 5$ , i.e. in the viscous sublayer), where

$$U^+ = z^+, \quad (1.2)$$

as required in the limit  $z^+ \rightarrow 0$ . The second applies farther from the wall while  $\eta$  remains

small:

$$U^+ = \frac{1}{\kappa} \ln(z^+) + B, \quad (1.3)$$

where  $\kappa$  and  $B$  are traditionally referred to as the von Kármán and additive constants (Marusic *et al.* 2013), respectively, although recent studies suggest that they should be regarded as coefficients that may depend on flow and boundary conditions (Monkewitz & Nagib 2023). This classical logarithmic law is observed in the overlap region of canonical high- $Re_\tau$  TBLs and has been studied extensively (Marusic *et al.* 2010).

Between the viscous sublayer and overlap region lies the buffer region, where neither scaling law applies exclusively. Its functional form is not well defined physically, and some studies (Long & Chen 1981) have further identified ‘mesolayers’ between the buffer and overlap regions. Accordingly, many studies have sought to combine the two classical scaling laws into a single expression for the near-wall mean velocity. For example, Van Driest (1956) derived a shear-stress relation that, when integrated, yields an integral expression for the streamwise velocity, although its practical use is not straightforward. Alternative expressions, such as those of Spalding (1961) and Musker (1979), provide a single representation for the viscous sublayer and buffer regions (collectively termed the ‘inner’ region) and asymptotically recover the logarithmic law with increasing wall-normal distance.

Following these ideas, many composite formulations take the form

$$U^+ = U_{\text{inner}}^+(z^+) + U_{\text{overlap}}^+(z^+, \eta) + U_{\text{wake}}^+(\eta, \Pi), \quad (1.4)$$

where separate analytical expressions describe the inner, overlap and wake regions of the TBL (see Chauhan *et al.* 2009). If the boundary-layer thickness and friction velocity are known, these formulations contain only one free parameter,  $\Pi$ , which may be obtained by fitting the composite profile to the measured mean velocity profile. Such formulations are therefore referred to here as *one-parameter composite profiles*. They typically provide good fits for ‘well-behaved’ canonical TBLs (i.e. smooth-wall, zero-pressure-gradient (ZPG) flows with minimal history effects; see Chauhan *et al.* 2009), although some limitations remain.

For example, the boundary-layer thickness used in these formulations does not always correspond to a commonly or easily measured quantity (e.g.  $\delta_{99}$ ), and is sometimes treated as an additional fitting parameter. Further uncertainty arises in the wake region. The original wake function,  $\mathcal{W}$ , introduced by Coles (1956) was sinusoidal, such that the wake contribution was written as

$$U_{\text{wake}}^+ = \frac{2\Pi}{\kappa} \mathcal{W}(\eta). \quad (1.5)$$

Subsequent studies have instead used exponential functions (Chauhan *et al.* 2007; Nickels 2004), polynomial functions (Jones *et al.* 2001), and other physically motivated models (for example, based on turbulent/non-turbulent interface (TNTI) interactions; Krug *et al.* 2017). Although these forms can produce good fits for particular TBLs, ambiguity regarding a generally applicable wake function persists.

For pressure-gradient (PG) TBLs specifically, the mean velocity profile depends not only on Reynolds number but also on both the local streamwise PG (Nagano *et al.* 1998; Deshpande *et al.* 2023; Harun *et al.* 2013; Drózdź *et al.* 2020; Monty *et al.* 2011) and the upstream PG history (Bobke *et al.* 2017; Pozuelo *et al.* 2022; Romero *et al.* 2023; Vinuesa *et al.* 2017). However, there is currently no established mathematical framework for explicitly describing the mean velocity profile of generic PG TBLs. Although one-parameter composite profiles were not intended only for canonical flows, they generally do not describe non-canonical TBLs well, including certain regimes of streamwise PG and/or surface roughness. For example, in PG flows without a wake region (e.g. sink flows), the overlap expression in (1.4) grows unboundedly, whereas the mean velocity should approach a constant value at

the boundary-layer edge (i.e.  $U^+ \rightarrow U_\infty^+$  as  $\eta \rightarrow 1$ ). These limitations have motivated new composite formulations for specific non-canonical TBL classes, including generic PG TBLs (Nickels 2004).

Accounting for streamwise PGs in a composite mean velocity formulation requires at least one additional free parameter beyond  $\Pi$ , yielding a *two-parameter composite profile*. Here the local PG is quantified using Clauser's pressure-gradient parameter,

$$\beta = \frac{\delta^*}{\tau_w} \left( \frac{dP}{dx} \right),$$

where  $\delta^*$  denotes the displacement thickness and  $dP/dx$  the streamwise gradient of the static pressure. The local PG strength may also be expressed using viscous scaling alone:

$$p_x^+ = \frac{\nu}{\rho u_\tau^3} \left( \frac{dP}{dx} \right). \quad (1.6)$$

This viscous-scaled PG parameter,  $p_x^+$ , is important because it arises naturally in composite formulations, specifically in the inner-region expression, through a Taylor-series expansion of the boundary-layer equations near the wall (Nickels 2004). The PG-related terms in this expansion are often neglected because  $p_x^+$  is small in high- $Re_\tau$  TBLs ( $p_x^+ = \beta/\delta^{*+}$ ) and/or in flows with low-to-moderate PGs. However, these terms become significant in low- $Re_\tau$  PG TBLs and in flows subjected to strong PGs (Nickels 2004).

Accordingly, Nickels (2004) reintroduced the  $p_x^+$ -dependent terms and introduced a new parameter,  $z_c^+ = z_c U_\tau / \nu$ , into the inner and overlap expressions of the composite profile:

$$U^+ = U_{\text{inner}}^+(z^+, p_x^+, z_c^+) + U_{\text{overlap}}^+(z^+, p_x^+, z_c^+, \eta) + U_{\text{wake}}^+(\eta, \Pi), \quad (1.7)$$

The parameter  $z_c^+$ , referred to as the 'sublayer thickness', accounts for PG-induced changes to the inner and overlap regions of the mean velocity profile. The details of this formulation are given by Nickels (2004); here, only the key features relevant to the present study are summarised. The contributions of the inner, overlap, and wake terms in Nickels' formulation are shown in figure 1, together with the effects of varying  $z_c^+$  and  $p_x^+$ . The shape of the inner-region profile depends on the magnitude of  $p_x^+$  through the inclusion of the PG-related terms from the Taylor expansion (figure 1a), while the inner-region profile asymptotes to a constant value equal to the sublayer thickness,  $z_c^+$  (figure 1b).

A fundamental relationship between  $p_x^+$  and  $z_c^+$  can be obtained by following the arguments of Clauser (1954) and Van Driest & Blumer (1963), which introduce a critical Reynolds number,

$$R_c = z_c U_{\tau,c} / \nu,$$

where  $z_c$  is a critical wall-normal location at which the sublayer becomes unstable, and  $U_{\tau,c} = \sqrt{\tau(z = z_c) / \rho}$ . Within Nickels' framework, the total shear stress near the wall may be written as

$$\frac{\tau}{\tau_w} = -\overline{uw}^+ + \frac{\partial U^+}{\partial z^+} \approx 1 + p_x^+ z_c^+, \quad (1.8)$$

and substitution into the critical-Reynolds-number relation yields

$$p_x^+ z_c^{+3} + z_c^{+2} - R_c^2 = 0. \quad (1.9)$$

Here,  $R_c$  is assumed to be universal for wall-bounded flows, with a value of approximately 12.

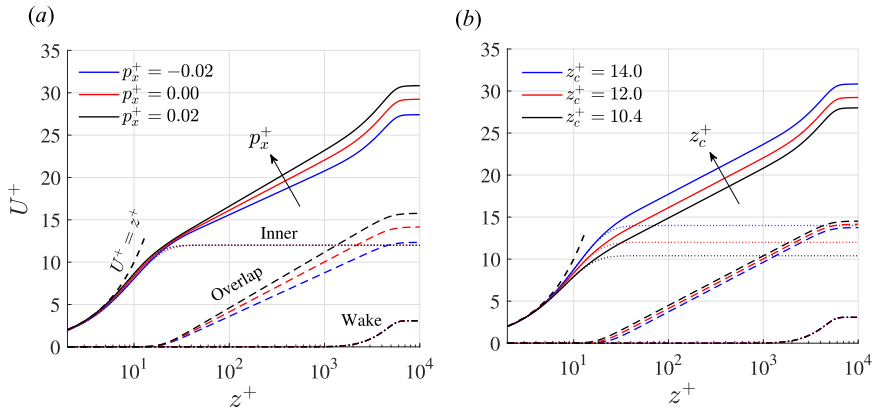


Figure 1: Contributions of the inner, overlap and wake expressions from Nickels (2004) as a function of (a)  $p_x^+$  and (b)  $z_c^+$ . The composite mean velocity profile (solid lines) is the sum of the three individual expressions. A baseline dataset with  $Re_\tau = 5000$  was used to generate these profiles.

Nickels also showed that in the high-Reynolds-number limit  $z_c^+$  is directly related to the classical additive constant  $B$  of the logarithmic law, indicating that  $z_c^+$  plays an important role in describing deviations from classical logarithmic scaling in PG TBLs. The formulation further prescribes changes in the von Kármán coefficient proportional to  $p_x^+$ , suggesting that at sufficiently high Reynolds numbers the von Kármán coefficient remains quasi-invariant and asymptotes to a constant value,  $\kappa$ . In addition, the overlap expression in (1.7) does not grow unboundedly (figure 1), thereby avoiding the non-physical behaviour of some composite profiles, particularly in flows with a weak or absent wake region such as sink flows.

These predictions were tested experimentally in Part 1, where the universality of  $\kappa$  and the dependence of the additive constant,  $B$ , on  $\beta$  were investigated using a methodology that imposed moderate APG conditions with minimal PG-history effects at high  $Re_\tau$ . The results showed that, at high  $Re_\tau$ ,  $\kappa$  remained invariant within experimental uncertainty, while  $B$  decreased systematically with both local PG strength and PG history, consistent with the general framework of Nickels (2004).

In summary, Nickels' formulation may be categorised as a *two-parameter composite profile*, with free parameters  $z_c^+$  and  $\Pi$  accounting for variations in streamwise PG and Reynolds number. In practice, however, as with one-parameter composite profiles,  $\delta$  is often treated as an additional fitting parameter. Moreover, although Nickels' formulation was developed for generic PG TBLs, it does not explicitly account for PG history, and it does not adequately describe the mean velocity profile of high-Reynolds-number PG TBLs in all cases, since  $p_x^+$  is a *local* and *viscous-scaled* parameter, as demonstrated further in §3. For example, in the wake region, PG history was found in Part 1 to modify both the vertical displacement of the mean velocity, through changes in  $\Pi$  (see also Preskett *et al.* 2025), and the horizontal stretching of the wake profile, through changes in its  $\eta$  dependence. Similarly, in the overlap region, PG history introduces additional deviations from the  $\beta$ -based trend observed for the additive constant in Part 1. These observations suggest that at least one additional parameter is required to describe a broader range of PG TBLs, particularly those at high  $Re_\tau$  or influenced by substantial upstream PG histories.

Motivated by the framework of Nickels (2004) and the findings of Part 1, the growing database of APG TBLs in the literature provides a foundation for developing a more robust composite profile for generic APG TBLs. Past experimental and numerical investigations (e.g. Nagano *et al.* 1998; Monty *et al.* 2011; Bobke *et al.* 2017; Pozuelo *et al.* 2022; Sanmiguel Vila

*et al.* 2017; Perry *et al.* 2002; Preskett *et al.* 2025; Zarei *et al.* 2026) have provided new insight into the behaviour of the mean velocity profile across a wide range of Reynolds numbers and APG conditions. Building on these datasets and physical insights, the present study develops a composite mean velocity profile formulation applicable across a broad range of Reynolds numbers and APG conditions while accounting for PG history effects with minimal additional complexity. Analysis of the available datasets indicates that a two-parameter composite profile is insufficient to describe the range of PG TBL behaviour considered here. Accordingly, the formulation of Nickels (2004) is extended by introducing one additional parameter required to capture these effects, yielding a *three-parameter composite profile*.

The resulting formulation also provides several practical utilities. In particular, it enables estimation of  $U_\tau$  and  $\delta$  for APG TBL datasets in which these quantities are difficult to measure experimentally, especially for high  $Re_\tau$  TBLs or when PG histories are minimal or well controlled. The analytical form of the profile further allows evaluation of quantities involving wall-normal derivatives of the mean velocity, such as the indicator function, which are often difficult to obtain from experimental data. Finally, the additional parameter introduced to account for PG history effects can be interpreted in terms of an ‘effective’ local pressure gradient, providing new physical insight into the development of APG TBLs.

The remainder of the paper is organised as follows. Section 2 introduces the datasets used to assess and refine the composite profile formulation. Section 3 examines the limitations of existing composite profiles and motivates the modifications introduced here. Section 4 presents the new composite profile formulation and the associated fitting procedure. Section 5 evaluates the accuracy of the formulation and interprets trends in the fitted parameters across the compiled datasets. Section 6 discusses practical utilities of the composite profile for analysing APG TBL datasets.

## 2. Datasets

To assess the robustness of the proposed composite profile across a broad range of flow conditions, a carefully selected compilation of APG TBL datasets from the literature is considered. These datasets span more than three decades of experimental and numerical investigations and include well-resolved large-eddy simulations (LES) and direct-numerical simulations (DNS), together with experimental measurements, with and without PG history effects, covering a broad range of  $\beta$  and  $Re_\tau$ , as listed in table 1. Additional datasets (e.g. Marusic *et al.* 2015; Örlü & Schlatter 2013; Li *et al.* 2021) are also considered to highlight the influence of varying tripping or surface roughness conditions, which are distinct from PG-related influences. Considering APG TBLs both with and without pronounced PG history effects is a key aspect of the database assembled here, enabling the influence of upstream PG history to be decoupled from the effects of local flow conditions for parameters of the composite profile, such as  $z_c^+$ . This compilation of datasets, together with the composite profile framework described below, also provides a useful means of contextualising the effects of different PG histories across studies reported in the literature.

## 3. Formulation of a new composite profile for APG TBLs

To motivate key modifications to existing composite formulations for PG TBLs, the profile of Nickels (2004) is applied to several representative datasets from table 1. This assessment examines its accuracy and limitations across different flow conditions and across the various regions of the TBL. Specifically, the formulation of Nickels (2004) is fitted to high-resolution ZPG numerical data from Eitel-Amor *et al.* (2014), high- $Re_\tau$  APG experimental data from Zarei *et al.* (2026), and APG LES data with PG history effects from Bobke *et al.* (2017),

Reference	Database	$\beta$	$Re_\tau$	Cases	Symbol
Marusic & Perry (1995)	EXP	0-5	2840-4170	6	▲
Nagano <i>et al.</i> (1998)	EXP	0.77-5.32	420-600	3	▲
Monty <i>et al.</i> (2011)	EXP	0-1.52	2170-2970	2	▲
Örlü & Schlatter (2013)	EXP	0	1150-1970	3	▲
Eitel-Amor <i>et al.</i> (2014)	LES	0	1200-3140	4	▲
Marusic <i>et al.</i> (2015)	EXP	0	2820-13500	12	▲
Bobke <i>et al.</i> (2017)	LES	1.03-1.64	490-770	2	◆
Yoon <i>et al.</i> (2018)	DNS	1.45	830	1	◆
Sanmiguel Vila <i>et al.</i> (2020)	EXP	0-2.19	1430-5070	9	◆
Volino (2020)	EXP	0-6.6	1060-1450	8	◆
Li <i>et al.</i> (2021)	EXP	0	8610-23930	8	▼
Pozuelo <i>et al.</i> (2022)	LES	1.03-1.65	490-770	2	◆
Romero <i>et al.</i> (2022)	EXP	0.9-1.77	7100-7770	5	◆
Gungor <i>et al.</i> (2024)	DNS	0-0.2	860-1520	2	▼
Preskett <i>et al.</i> (2025)	EXP	0	6840-9440	6	▼
Zarei <i>et al.</i> (2026)	EXP	0-1.47	4000-10680	23	See Part 1

Table 1: Summary of flow conditions and symbols for the datasets considered in this study.

as shown in figure 2. The two-character designations for each profile correspond to specific cases listed in table 1, with nomenclature and specific details of individual cases documented in Appendix A.

Starting with the well-resolved ZPG dataset of Eitel-Amor *et al.* (2014) (figure 2a), the composite profile accurately captures the mean velocity in the overlap region and near the wall ( $z^+ < 10$ ). However, visible discrepancies remain in the buffer (inset I) and wake (inset II) regions. The discrepancy in the buffer region arises from a velocity overshoot relative to the overlap-region scaling (i.e. the classical logarithmic law), which has been observed in both experimental and numerical studies (Monkewitz *et al.* 2007) but is not captured by the inner-region expression in (1.7).

In the wake region, discrepancies arise when the boundary-layer thickness ( $\delta$ ) is not treated as a fitted parameter. In the present study,  $\delta$  is instead defined using the physically motivated approach derived from the skewness profile of the mean streamwise velocity fluctuations, and turbulent/non-turbulent interface framework of Lozier *et al.* (2025). Applying this independently determined  $\delta$  within the formulation of Nickels (2004) reveals that the wake function in (1.7) is not well suited to adopt this definition, as demonstrated consistently in figures 2(a–c). Nickels (2004) also noted this limitation; allowing  $\delta$  to vary as a fitted parameter introduced at least a 3% difference relative to the  $\delta_{98.5}$  definition, which may become larger when alternative definitions of  $\delta$  are used.

For the APG datasets, additional discrepancies appear in the overlap region for cases with strong PG history effects (inset III, figure 2b) or at high Reynolds number (inset V, figure 2c). These deviations arise from the overlap formulation of Nickels (2004), which relates shifts in the mean velocity to  $p_x^+$ . Because  $p_x^+$  diminishes with increasing  $Re_\tau$  (irrespective of the magnitude of  $dP/dx$ ) and reflects only the local PG, it does not capture the cumulative influence of PG history.

The discrepancy in the wake region is particularly pronounced for the case with strong PG history effects (inset IV, figure 2b). This behaviour is consistent with the findings of Part 1, which showed that PG history significantly modifies both the magnitude and the distribution of the mean velocity profile in the wake region.

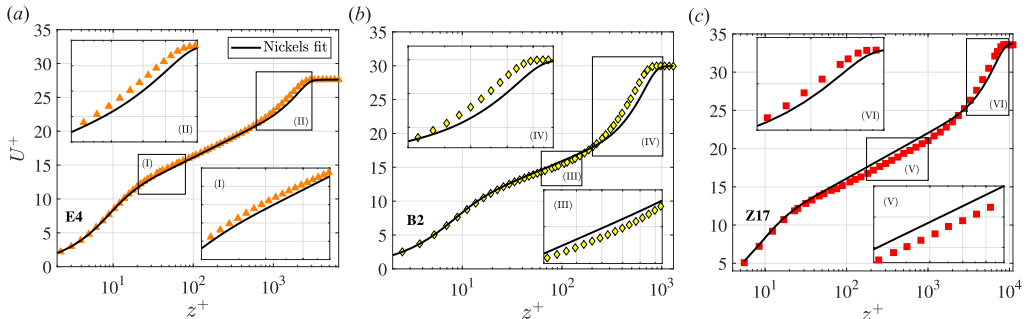


Figure 2: Mean velocity data and corresponding composite profile (1.7) for (a) a well-resolved LES ZPG dataset, (b) an APG dataset influenced by history effects, and (c) a high- $Re_\tau$  APG dataset with minimal PG history.

### 3.1. The new composite profile formulation

The observations described above motivate modifications to the formulation of Nickels (2004). Specifically, the present formulation introduces a velocity overshoot in the inner region, reformulates the wake function to be consistent with the physically motivated definition of  $\delta$  adopted here, and incorporates recent physical insights regarding pressure-gradient effects in the overlap region (at high  $Re_\tau$ ) and PG-history effects in the wake region.

Accordingly, we propose a modified composite profile expressed as

$$U^+ = U_{\text{inner}}^+(z^+, p_x^+, z_c^+) + U_{\text{overlap}}^+(z^+, p_x^+, z_c^+, \eta, C_{H_w}) + U_{\text{wake}}^+(\eta, C_{H_w}, \Pi). \quad (3.1)$$

The specific modifications to each component of the formulation are described below.

#### 3.1.1. Addition of a wake-stretching parameter

An additional parameter,  $C_{H_w}$ , is introduced as a ‘wake-stretching’ parameter to account for PG-history effects observed in the wake region. The coefficients in the wake function are also revised to ensure consistency with the boundary-layer thickness definition of Lozier *et al.* (2025). Accordingly, the outer-scaled wall-normal coordinate  $\eta$  is rescaled within the wake-region expression ( $U_{\text{wake}}^+$ ), resulting in an effective coordinate,

$$\eta_{\text{eff}} = 1.455 C_{H_w} \eta.$$

#### 3.1.2. Addition of an overshoot function

To account for the velocity overshoot observed in the buffer region, a Gaussian-type function is introduced following the approach of Monkewitz *et al.* (2007) and Chauhan *et al.* (2009), who incorporated a similar term into the inner-region expression of Musker (1979). The overshoot function is written as

$$f(z_c^+) \exp\left(\frac{-\ln^2(z^+/38)}{0.835}\right), \quad (3.2)$$

where  $f$  represents the maximum overshoot relative to the baseline profile of Musker (1979). For ZPG flow,  $f \approx 0.2$ , consistent with the findings of Chauhan *et al.* (2009). However, this value depends on the pressure gradient (i.e. varies with  $z_c^+$ ), as demonstrated in appendix B.

The contribution of the overshoot function is restricted to the inner region,  $9 \leq z^+ \leq 150$ , with its maximum occurring at  $z^+ = 38$ . This ensures that the inner-region expression

asymptotes to  $U^+ = z_c^+$  with increasing  $z$  (figure 3), consistent with the framework of Nickels (2004) and maintaining compatibility with the overlap-region formulation.

### 3.2. Linking local and upstream PGs to $z_c^+$

As demonstrated in Part 1 and by Bobke *et al.* (2017), PG-history effects can produce differences in the overlap-region mean velocity profiles of APG TBLs even when the local flow conditions ( $Re_\tau$  and  $\beta$ ) are matched. These differences appear primarily as variations in the additive constant  $B$  (or equivalently  $z_c^+$ , see Nickels 2004). To capture this behaviour, we introduce the concept of an effective pressure-gradient parameter,

$$\beta_{\text{eff}} = \beta C_{H_i},$$

which combines the local PG parameter,  $\beta$ , with a PG-history parameter,  $C_{H_i}$ , to represent the combined influence of local and upstream pressure gradients on the inner and overlap regions.

Importantly,  $C_{H_i}$  is not introduced as an additional free parameter of the composite profile. Rather, it is obtained from the fitting process and provides a means of linking local and upstream PG effects to  $z_c^+$ , thereby offering physical insight into the flow conditions experienced by the TBL. To model this relationship, we follow the framework of Nickels (2004), as described by (1.8) and (1.9). While  $p_x^+$  plays an important role in the near-wall shear-stress expression for APG TBLs (1.8) (particularly for  $z^+ < 5$ ), the resulting model for the sublayer thickness (1.9) does not capture the changes in  $z_c^+$  (or equivalently  $B$ ) observed for high- $Re_\tau$  TBLs with moderate APGs in Part 1.

Accordingly, we propose that  $z_c^+$  is more appropriately described as a function of  $\beta_{\text{eff}}$ , consistent with the results of Part 1 and previous studies. This leads to a modified form of (1.9):

$$c \beta_{\text{eff}} z_c^{+3} + z_c^{+2} - R_c^2 = 0, \quad (3.3)$$

whose root predicts  $z_c^+$  for a given  $\beta_{\text{eff}}$ . This model yields excellent agreement with experimental data for both low- and high- $Re_\tau$  APG TBLs when  $c = 0.0145$ , as demonstrated by the dashed line in figure 8(a).

The history parameter  $C_{H_i}$  can then be expressed in terms of  $z_c^+$  and  $\beta$  using (3.3):

$$\begin{aligned} C_{H_i} &= \frac{144 - z_c^{+2}}{c\beta z_c^{+3}} \quad \text{for } \beta \neq 0 \\ C_{H_i} &= \frac{12}{z_c^+} \quad \text{for } \beta = 0 \end{aligned} \quad (3.4)$$

To avoid the singularity that arises for nominally ZPG cases ( $\beta = 0$ ), the second expression compares the fitted  $z_c^+$  directly with the canonical ZPG value  $z_c^+ = 12$ . For APG TBLs with minimal upstream PG-history effects, both history parameters introduced here should be approximately unity ( $C_{H_i} \approx 1$  and  $C_{H_w} \approx 1$ ). Deviations from unity therefore indicate a significant influence of PG history on the TBL.

Notably,  $C_{H_i}$  and  $C_{H_w}$  are independent parameters that can be interpreted in terms of the characteristic time scales associated with different PG effects. Specifically,  $C_{H_i}$  reflects the relatively rapid response of the inner region to changes in PG conditions, whereas  $C_{H_w}$  represents the slower adjustment of the wake region, consistent with the observations reported in Part 1.

Incorporating these modifications, the proposed composite profile formulation becomes

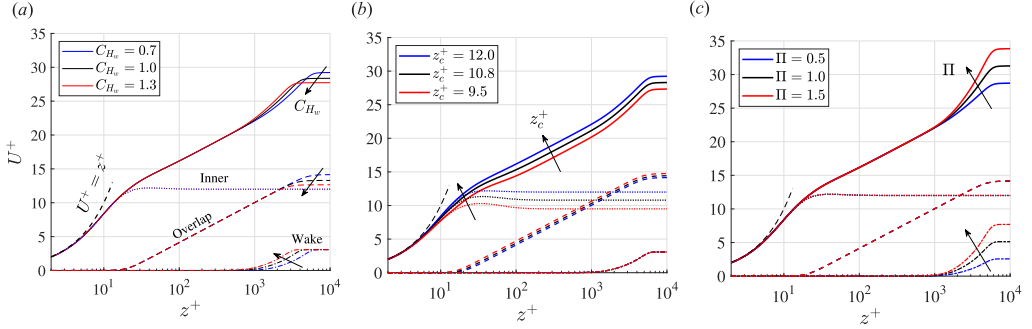


Figure 3: Contributions of the inner (3.5), overlap (3.6) and wake (3.7) expressions to the present composite profile as a function of (a) the wake history factor  $C_{H_w}$ , (b)  $z_c^+$ , and (c)  $\Pi$ . A reference dataset with  $Re_\tau = 5000$  was used to generate these profiles.

$$U_{\text{inner}}^+ = z_c^+ \left[ 1 - \left( 1 + 2 \left( \frac{z^+}{z_c^+} \right) + \frac{1}{2} (3 - p_x^+ z_c^+) \left( \frac{z^+}{z_c^+} \right)^2 - \frac{3}{2} p_x^+ z_c^+ \left( \frac{z^+}{z_c^+} \right)^3 \right) e^{-\frac{3z^+}{z_c^+}} \right] + \left( 0.23 + 0.5 \tanh \left( 31 \frac{144 - z_c^{+2}}{z_c^{+3}} \right) \right) \exp \left( \frac{-\ln^2(z^+/38)}{0.835} \right) \quad (3.5)$$

$$U_{\text{overlap}}^+ = \frac{\sqrt{1 + p_x^+ z_c^+}}{6\kappa} \ln \left( \frac{1 + (0.6(z^+/z_c^+))^6}{1 + \eta_{\text{eff}}^6} \right); \quad (3.6)$$

$$U_{\text{wake}}^+ = \frac{2\Pi}{\kappa} \left( 1 - \exp \left( \frac{-15(\eta_{\text{eff}}^4 + \eta_{\text{eff}}^8)}{1 + 15\eta_{\text{eff}}^3} \right) \right). \quad (3.7)$$

Figure 3 illustrates the influence of the three free parameters ( $C_{H_w}$ ,  $z_c^+$ , and  $\Pi$ ) on the resulting composite mean velocity profile. Variations in  $C_{H_w}$  and  $\Pi$  primarily reshape the wake region, influencing both the extent and magnitude of the wake. In contrast, variations in  $z_c^+$  modify the overlap region (through shifts in the mean velocity) and the inner region (through the magnitude of the buffer-region overshoot and the near-wall profile shape).

### 3.3. Note for high-Reynolds-number TBLs

In the high- $Re_\tau$  limit, the proposed composite profile formulation simplifies, particularly in the overlap region. Specifically, as  $Re_\tau \rightarrow \infty$ ,  $p_x^+ \rightarrow 0$  and  $\eta_{\text{eff}} \rightarrow 0$ , while  $z^+ \rightarrow \infty$  (since  $\delta^+ \rightarrow \infty$ ). In this limit, the inner-region expression asymptotes to  $U^+ = z_c^+$  for  $z^+ \gg z_c^+$ . Consequently, the overlap-region expression (3.6) reduces to

$$U^+ = \frac{1}{\kappa} \ln(z^+) - \underbrace{\frac{1}{\kappa} \ln(z_c^+/0.6)}_B + z_c^+, \quad (3.8)$$

which has the form of the classical logarithmic law. Here  $\kappa$  remains constant, while the additive constant  $B$  depends only on  $z_c^+$  (i.e. the pressure gradient), consistent with the results of Part 1. For ZPG TBLs, when  $z_c^+ = 12$ , (3.8) reduces to the classical log-law with  $\kappa = 0.39$  and  $B = 4.3$ , consistent with Marusic *et al.* (2013).

### 3.4. Fitting method

We now outline practical considerations for applying the proposed composite mean velocity profile to APG TBL datasets. The primary inputs may be expressed in normalised form as  $U^+$ ,  $z^+$ ,  $Re_\tau$  and  $p_x^+$  (or equivalently in dimensional form as  $U$ ,  $z$ ,  $U_\tau$ ,  $\delta$ ,  $dP/dx$ ,  $\nu$  and  $\rho$ ). The three parameters optimised when fitting the composite profile to a dataset are the sublayer thickness  $z_c^+$  (which also determines  $\beta_{\text{eff}}$  and  $C_{H_i}$ ), together with the wake parameters  $\Pi$  and  $C_{H_w}$ .

For all cases considered here, the parameters were obtained using a nonlinear least-squares curve-fitting procedure applied to the measured mean velocity profiles. To facilitate application of this method, an example implementation is provided as a [notebook](#). Normalised mean velocity data, together with the corresponding flow parameters described above, can be supplied as inputs. The notebook then performs the nonlinear fit to determine the optimal values of the three free parameters in the composite profile formulation (3.1) and plots the resulting fitted profile.

The fitting procedure was tested for all datasets considered in this study (table 2) to confirm that the optimisation remained robust across a wide range of flow conditions. In addition, for TBLs with minimal or well-controlled PG history effects (i.e.  $C_{H_i} = C_{H_w} = 1$ ), the composite profile may alternatively be used to estimate  $U_\tau$  and  $\delta$ , as discussed in §5. An implementation of this procedure is also provided in a separate [notebook](#), where dimensional mean velocity data can be supplied when  $U_\tau$  and  $\delta$  are not known a priori.

## 4. Quality and interpretation of the new composite profile

In this section, the accuracy of the new composite profile is evaluated using a range of ZPG and APG datasets, with and without PG history effects, and trends in the optimised fitting parameters are examined. Appendix A provides a complete list of parameters obtained from the fitting procedure for the cases considered.

The composite profile is first fitted to a series of ZPG datasets with well-controlled PG histories, as shown in figure 4. The optimised profiles match the mean velocity data well across all cases and regions of the TBL. The resulting fitting parameters confirm that  $z_c^+ = 12$  for ZPG TBLs, independent of data resolution and database type (i.e. experimental or numerical), consistent with Nickels (2004). Moreover, the resulting history parameters are found to be  $C_{H_w} \approx C_{H_i} \approx 1$  for all cases, confirming that PG history effects are minimal.

Next, the composite profile is fitted to the high- $Re_\tau$  moderate-APG dataset with minimal PG history effects from Part 1, as shown in figure 5. These cases are of particular interest because they enable PG-related trends in the optimised fitting parameters to be examined without the additional influence of PG history effects. The profiles are presented using both linear and logarithmic scaling of the wall-normal distance ( $z^+$ ) to demonstrate the quality of the fit across all regions of the TBL. As with the ZPG datasets above, the resulting fitting parameters indicate that  $C_{H_w} \approx 1$  for these APG datasets, confirming minimal effects of PG history.

Finally, the composite profile is fitted to select APG datasets with varying PG history effects that span a broad range of  $Re_\tau$  and  $\beta$ , as shown in figures 6 and 7. For clarity, the experimental and numerical datasets are plotted separately in figure 6. The fitted composite profiles match the mean velocity data well in each case, and the optimised values of  $z_c^+$ ,  $C_{H_w}$ , and  $\Pi$  for these datasets are listed in appendix A.

For some datasets, the boundary-layer thickness  $\delta$  cannot be determined using the method of Lozier *et al.* (2025), due to the unavailability of skewness data. In such cases, the composite profile fitting procedure still provides optimised values of  $z_c^+$  and  $\Pi$ , together with an effective

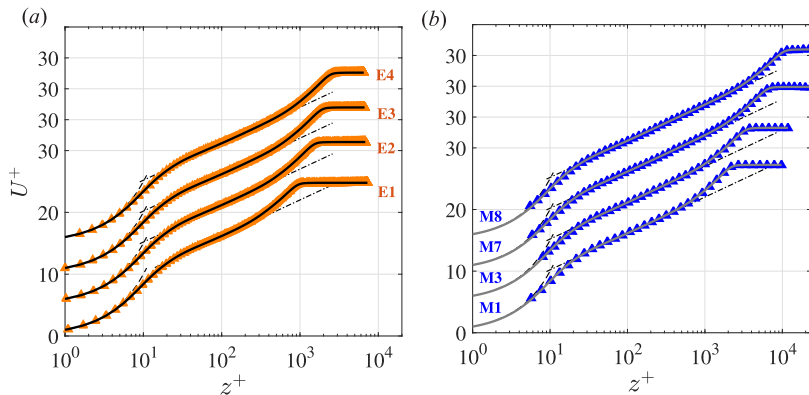


Figure 4: Validation of the new composite profile for ZPG TBLs with minimal PG history from (a) the low- $Re_\tau$  LES dataset of Eitel-Amor *et al.* (2014), and (b) the high- $Re_\tau$  dataset of Marusic *et al.* (2015). Individual profiles are offset by five units in the vertical direction. Dashed lines represent (1.2) and dash-dotted lines represent (1.3).

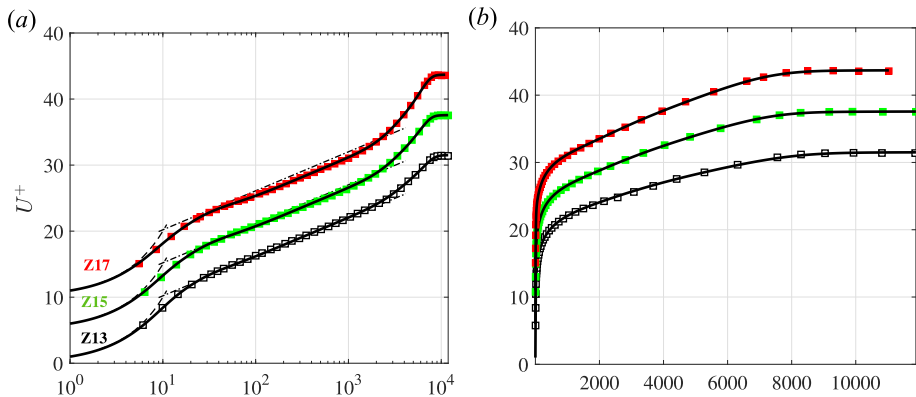


Figure 5: Validation of the new composite profile for high- $Re_\tau$  moderate-APG TBLs with minimal PG history effects from Part 1. The mean velocity profiles are plotted in both (a) logarithmic and (b) linear scaling to confirm the quality of the composite profile across all regions of the TBL. Dashed lines represent (1.2) and dash-dotted lines represent (1.3).

outer length scale  $\delta/C_{H_w}$ . The boundary-layer thickness  $\delta$  can then be estimated by assuming  $C_{H_w} = 1$ , or alternatively  $C_{H_w}$  can be estimated by assuming  $\delta = 1.25\delta_{99}$  (following Lozier *et al.* 2025). Despite this uncertainty, the fitted composite profiles continue to match the mean velocity data well, including cases with significant PG effects (figure 7).

Having established the accuracy of the composite profile across a broad range of APG TBL datasets, the fitting procedure was applied to all datasets considered in this study. The resulting parameters were then compiled to evaluate trends associated with pressure-gradient effects.

#### 4.1. Overlap region

We first examine trends in  $z_c^+$ , a key parameter governing the overlap-region behaviour of the mean velocity profile. As discussed by Nickels (2004) and demonstrated experimentally in Part 1,  $z_c^+$  determines the additive constant of the classical log-law and therefore controls the vertical shift of the overlap-region mean velocity profile. This parameter is expected to

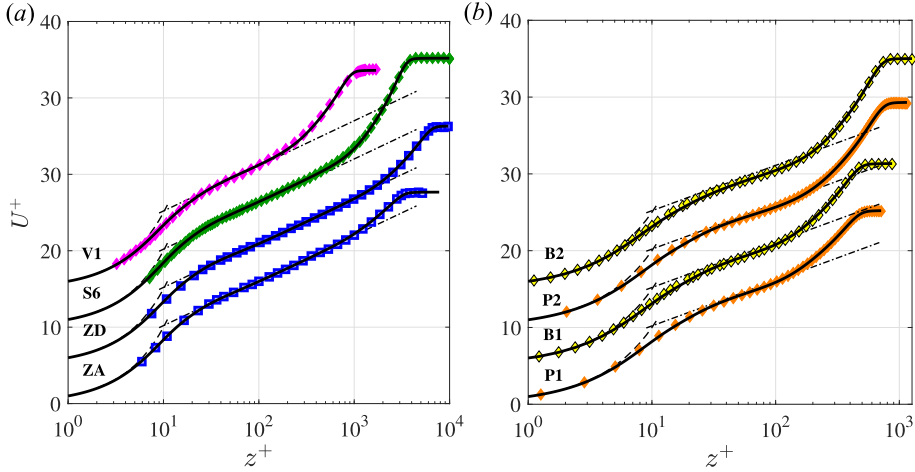


Figure 6: Validation of the new composite profile for a range of (a) experimental and (b) numerical APG TBL datasets with PG history effects. Dashed lines represent (1.2) and dash-dotted lines represent (1.3).

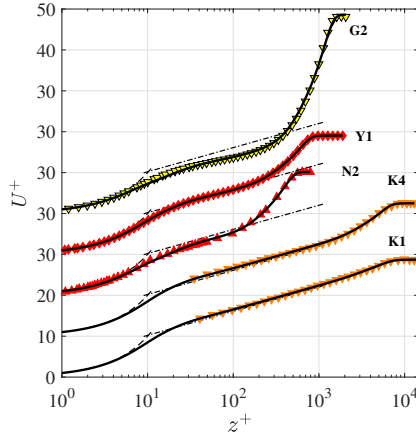


Figure 7: Validation of the new composite profile for additional APG TBL datasets where  $\delta$  is not known. Dashed lines represent (1.2) and dash-dotted lines represent (1.3).

depend on the pressure gradient according to the model (3.3). The optimised values of  $z_c^+$  for cases with minimal PG history are plotted as a function of  $\beta$  in figure 8(a). Excellent agreement is observed between the  $z_c^+$  values obtained from the composite-profile fitting method (where  $C_{H_i} \approx 1$ ) and the tuned model (3.3), shown by the dashed black line in figures 8(a,b). Notably,  $z_c^+$  decreases systematically with increasing APG, independent of Reynolds number, consistent with the results of Part 1. These trends also follow the proposed  $\beta$ -dependent model (3.3) more closely than the original  $p_x^+$ -based model (1.9) of Nickels (2004) (not shown here).

We next consider cases with significant PG history effects, shown in figure 8(b). For these datasets, the optimised  $z_c^+$  values deviate from the model (3.3), indicating the influence of PG history and resulting in  $C_{H_i} \neq 1$ . Physically,  $C_{H_i}$  represents the cumulative influence of upstream pressure-gradient events on the overlap-region structure of the mean velocity profile. Values of  $C_{H_i} > 1$  correspond to cases where upstream PG development enhances

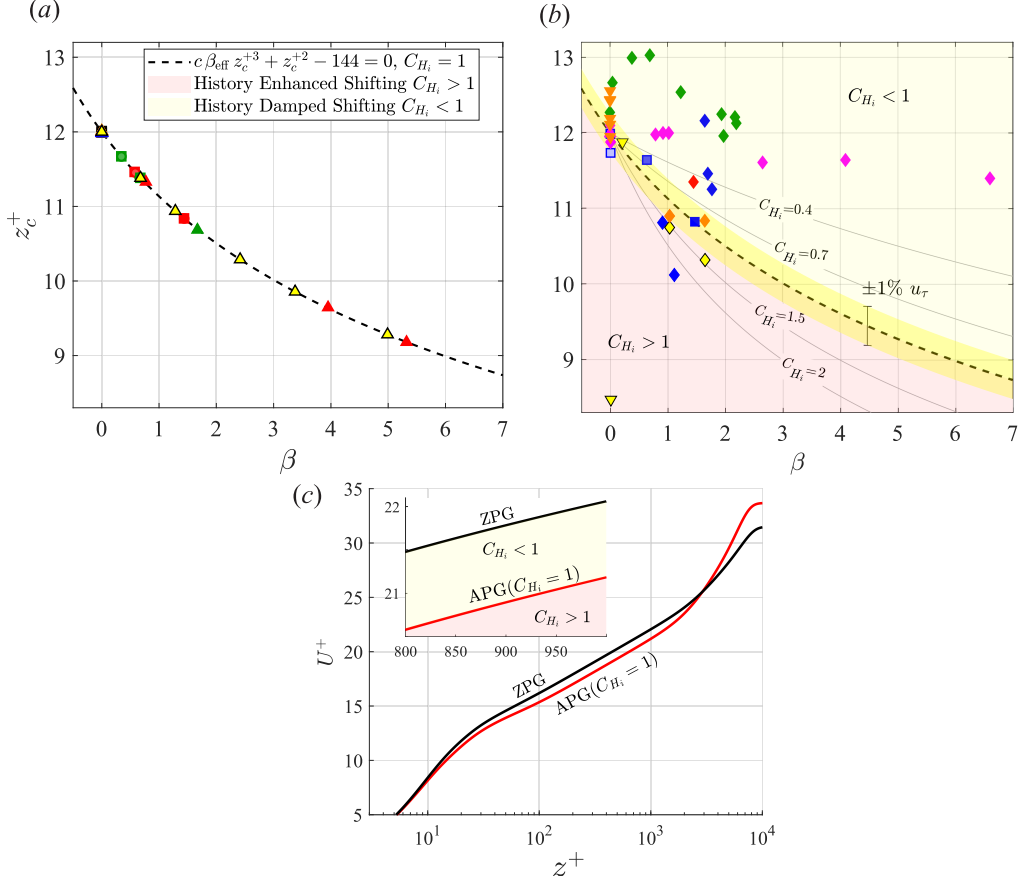


Figure 8: Variation of  $z_c^+$  with  $\beta$  for (a) cases with minimal PG history and (b) cases with PG history effects. The dashed line represents the proposed model (3.3), and the grey lines represent  $C_{H_i}$  levels. (c) Schematic of the mean velocity profile for a reference high- $Re_\tau$  ZPG and an APG dataset depicting ‘history-enhanced’ and ‘history-damped’ shifting behaviours.

the downward shift in the overlap region of the mean velocity relative to that predicted by the local PG alone, whereas  $C_{H_i} < 1$  indicates a relative upward shift arising from the upstream PG history (figure 8c). The patterns of  $z_c^+$  observed within individual datasets reflect the unique PG histories of each case (e.g. differences in the  $\beta(x)$  distributions arising from ramp or roof geometries in experiments). Minor deviations from the model curve that fall within experimental uncertainty should not necessarily be interpreted as significant PG history effects.

However, some cases show clear evidence of strong PG history influence. For example, the datasets of Gungor *et al.* (2024) and Preskett *et al.* (2025) correspond to nominally ZPG conditions ( $\beta = 0$  locally) but have experienced significant PG events upstream. These cases appear as the yellow and orange downward triangles in figure 8(b), lying at  $\beta = 0$  but with  $z_c^+ \neq 12$ . Their corresponding mean velocity profiles are shown in figure 7(b), specifically case G2 from Gungor *et al.* (2024) ( $z_c^+ = 8.2$ ) and case Pr4 from Preskett *et al.* (2025) ( $z_c^+ = 12.6$ ), illustrating the non-canonical behaviour of these profiles despite locally ZPG conditions.

To aid interpretation of  $C_{H_i}$ , we consider the schematic mean velocity profiles of reference

high- $Re_\tau$  ZPG and APG TBLs with minimal PG history shown in figure 8(c). The APG profile exhibits the expected downward shift relative to the ZPG profile in the overlap region. When PG history effects are present (while maintaining the same local  $\beta$ ), the profile may instead lie between the reference ZPG and APG cases, corresponding to  $C_{H_i} < 1$ . We refer to this behaviour as *history-damped shifting*. Conversely, the overlap-region shift may exceed that of the reference APG profile, corresponding to  $C_{H_i} > 1$ , which we term *history-enhanced shifting*. It is also noted that if the APG profile instead lies above the ZPG profile,  $C_{H_i} < 0$ .

Cases with  $C_{H_i} \neq 1$  can be mapped to an effective pressure-gradient parameter  $\beta_{\text{eff}}$  using the measured  $z_c^+$  and (3.3). Flows with matched  $\beta_{\text{eff}}$  therefore exhibit similar overlap-region behaviour (i.e. the same additive constant  $B$ ). In this way,  $\beta_{\text{eff}}$  may be interpreted as the effective pressure gradient experienced by the boundary layer after accounting for the influence of upstream PG development. This framework, therefore, provides a simple means of interpreting the combined influence of local and upstream PGs on the mean velocity profile.

These PG history effects become clearer when considering TBLs with matched local conditions ( $Re_\tau$  and  $\beta$ ) but different PG histories. The corresponding  $z_c^+$  values for such cases from the numerical datasets of Pozuelo *et al.* (2022) and Bobke *et al.* (2017), together with the high- $Re_\tau$  experimental dataset from Part 1, are shown in figures 9(a,b). In figure 9(a), differences in the upstream PG development (see inset  $\beta(x)$  distributions) produce clear differences in  $z_c^+$  despite matched local flow conditions. In other words, the local and upstream PGs combine to produce different effective pressure gradients  $\beta_{\text{eff}}$ . For the higher- $Re_\tau$  data points (labelled 2), the case of Pozuelo *et al.* (2022) exhibits history-damped shifting, whereas the case of Bobke *et al.* (2017) exhibits history-enhanced shifting, indicating a larger  $\beta_{\text{eff}}$ .

In figure 9(b), the cases labelled ZA and ZD were designed to introduce measurable PG history effects relative to the reference minimal-history cases (ZA-ref. and ZD-ref.) from Part 1. For ZA, an imposed upstream APG perturbation produces history-enhanced shifting relative to the reference ZPG case (ZA-ref.), corresponding to  $\beta_{\text{eff}} > 0$ . In contrast, delayed APG development in ZD relative to the reference APG case (ZD-ref.) leads to history-damped shifting, although  $z_c^+$  remains less than the canonical ZPG value of 12 (i.e.  $\beta > \beta_{\text{eff}} > 0$ ). Finally, despite differences in upstream PG history, both ZE and ZE-ref. exhibit overlap-region shifts consistent with the local  $\beta$ , following (3.3).

Together, these observations demonstrate that the composite profile, fitting procedure and PG-history framework proposed here provide a consistent way to describe the combined influence of local and upstream PGs across a wide range of APG TBLs. While the parameter  $C_{H_i}$  characterises PG-history effects on the overlap-region velocity shift, the wake region can exhibit additional history-dependent behaviour. We therefore next examine how PG history influences the wake structure through the parameter  $C_{H_w}$ .

#### 4.2. Wake region

The wake region can also be strongly influenced by both local and upstream pressure gradients (Bobke *et al.* 2017; Gungor *et al.* 2024; Preskett *et al.* 2025). In contrast to the inner and overlap regions, which adjust relatively rapidly to changes in the local flow conditions, the wake region evolves over longer streamwise development lengths and therefore retains a stronger memory of upstream PG events. This behaviour motivates the introduction of the wake-history parameter  $C_{H_w}$  in the composite profile formulation, which captures history-dependent stretching of the wake region mean velocity profile. Consequently, it is challenging to formulate a general wake function that accounts simultaneously for a wide range of local APGs and PG-history effects while also incorporating an independent measure of  $\delta$ . To demonstrate the robustness of the present composite formulation, both PG history parameters

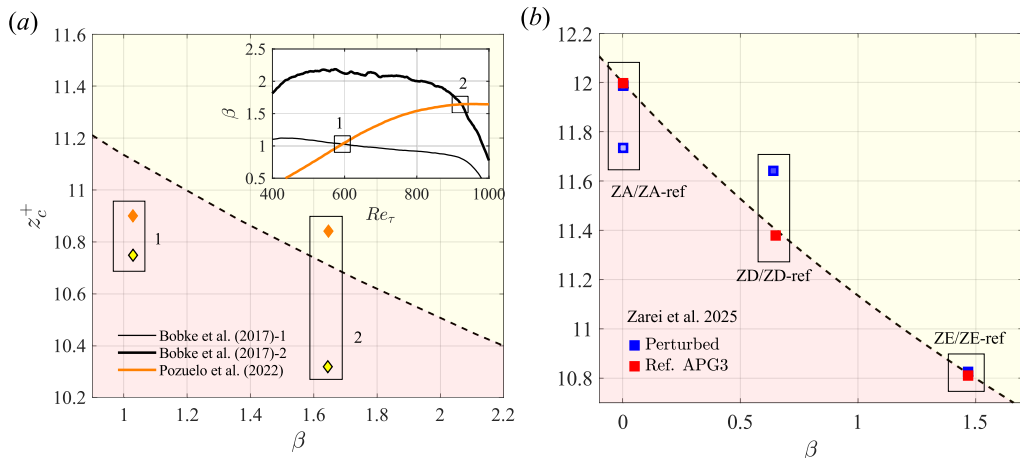


Figure 9: Variation of  $z_c^+$  with  $\beta$  for cases with matched local flow conditions ( $Re_\tau$  and  $\beta$ ) but different PG histories from the datasets of (a) Pozuelo *et al.* (2022) and Bobke *et al.* (2017), and (b) Zarei *et al.* (2026).

(i.e.  $C_{H_w}$  and  $C_{H_i}$ ) obtained from a subset of the datasets considered here are plotted as a function of  $Re_\tau$  in figure 10.

For cases with minimal PG history, including both experimental and numerical ZPG and APG datasets, the values of  $C_{H_w} \approx C_{H_i} \approx 1$  (within a 2% margin), largely independent of  $Re_\tau$  and  $\beta$ . This behaviour is consistent with previous studies, such as Krug *et al.* (2017) and Chauhan *et al.* (2009), which employed constant coefficients in their wake functions, although these were primarily valid for ‘well-behaved’ TBLs.

When PG history effects are present, deviations appear in both the wake parameter ( $C_{H_w}$ ) and the inner/overlap parameter ( $C_{H_i}$ ). This behaviour is evident for the cases ZA and ZD discussed in section 4.1. In some datasets, the influence of PG history is even more pronounced in  $C_{H_w}$  than in  $C_{H_i}$ , for example, the orange downward triangles corresponding to Preskett *et al.* (2025). This observation highlights the importance of also considering  $C_{H_w}$  when characterising PG history effects.

These results, therefore, justify the inclusion of  $C_{H_w}$  as a parameter in the present composite formulation. Without this parameter, the wake function cannot simultaneously reproduce the observed variations in the wake region mean velocity profiles across datasets with different PG histories, leading to systematic deviations in the wake region of up to  $\pm 20\%$  in the effective wake scaling.

Further, the results also highlight the importance of incorporating an independent measure of  $\delta$ , since the wake function can scale with both  $C_{H_w}$  and  $\delta$  through  $\eta_{\text{eff}} = 1.455 C_{H_w} z / \delta$ . This observation is consistent with Lozier *et al.* (2025), who showed that the ratio  $\delta / \delta_{99}$  (effectively a measure of wake stretching) remains nearly constant for TBLs with minimal PG history but deviates when PG history effects are present.

Finally, it should be noted that variations in tripping conditions or surface roughness perturbations can also influence the history parameters  $C_{H_w}$  and  $C_{H_i}$ , as discussed further in appendix C.

## 5. Utilities of the new composite profile

In addition to the framework for characterising PG history effects described in section 4, and the broader applications of well-resolved mean velocity profiles in resolvent analysis

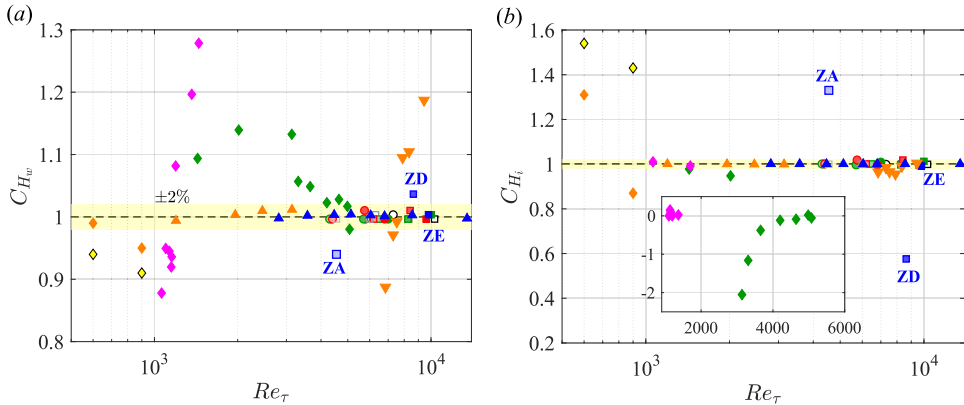


Figure 10: Variation of (a)  $C_{H_w}$  and (b)  $C_{H_i}$  for all datasets considered here.

or Reynolds-stress modelling, the new composite profile also provides practical utilities for analysing previously published and future APG TBL datasets.

### 5.1. Revisiting previous datasets

Accurate measurement of  $U_{\tau}$  and/or  $\delta$  is often challenging in APG TBL experiments, especially for those at high  $Re_{\tau}$ . Accordingly, one of the primary utilities of the proposed composite profile is to estimate these key boundary-layer characteristics from datasets in which they are not directly measured. To achieve this, the curve-fitting procedure described in section 3.4 is applied using the composite profile formulation together with (3.3). In this case, the inputs consist of the non-normalised mean velocity profile ( $U$  and  $z$ ), the streamwise pressure gradient ( $dP/dx$ ), and the fluid properties ( $\nu$  and  $\rho$ ). The PG history parameters must also be specified; for well-behaved TBLs, these typically satisfy  $C_{H_i} = C_{H_w} = 1$ . The fitting procedure then provides optimised values of  $U_{\tau}$ ,  $\Pi$ , and  $\delta$ , from which other boundary-layer properties may be determined.

To evaluate the accuracy of this approach, the method is applied to the datasets from Part 1, which are characterised by minimal PG history ( $C_{H_i} \approx C_{H_w} \approx 1$ ) and for which  $U_{\tau}$  and  $\delta$  were independently measured. The comparison is shown in figure 11. The values obtained from the composite-profile fitting procedure agree closely with the experimentally measured values and fall within the range of typical experimental uncertainties for all three quantities considered.

This demonstrates the utility of the composite profile as a tool for revisiting datasets in which direct measurements of  $U_{\tau}$  were not reported. As an example, the method is applied to the dataset of Marusic & Perry (1995), where  $U_{\tau}$  was originally estimated using the Clauser method and near-wall measurements were limited. Despite the absence of near-wall data, the composite profile matches the experimental velocity profiles well (figure 12a). Comparing the resulting friction velocities with those obtained using the Clauser method (figure 12b) reveals clear differences for cases with the highest  $\beta$ , while the ZPG case shows good agreement. This behaviour is expected, since the Clauser method is reliable primarily for canonical TBLs with negligible pressure gradients.

The optimised parameters obtained from this procedure are listed in table 2. In addition to providing improved estimates of the friction velocity, the composite profile also yields a well-resolved representation of the near-wall velocity profile, which was experimentally inaccessible for these cases (yellow-shaded region in figure 12b).

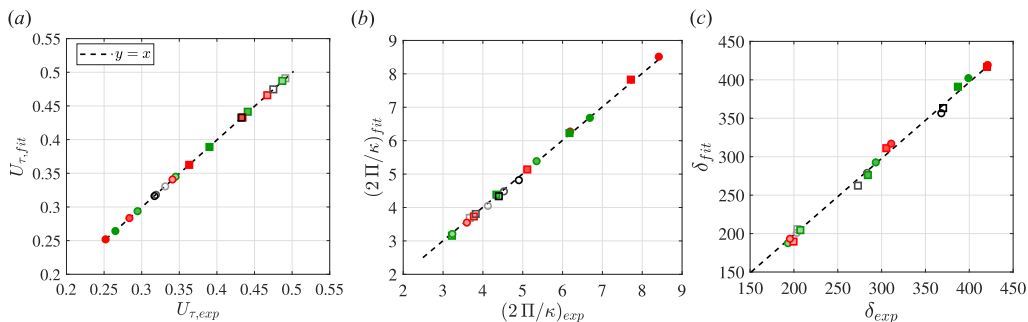


Figure 11: Comparison between fitted and directly measured values of (a) the friction velocity  $U_{\tau}$ , (b) the wake strength  $2\Pi/\kappa$ , and (c) the TBL thickness  $\delta$  for the datasets from Part 1.

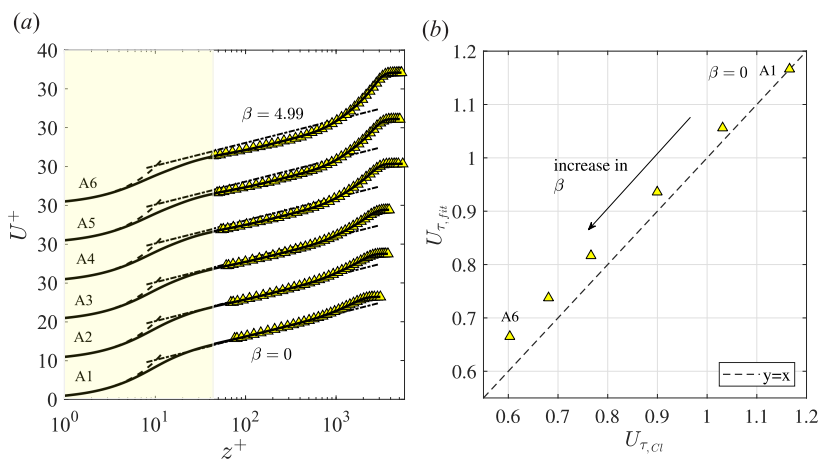


Figure 12: (a) Experimental mean velocity data and corresponding composite profiles from Marusic & Perry (1995). The yellow-shaded region indicates the near-wall extent, which was not measured experimentally. (b) Comparison of  $U_{\tau}$  values obtained from the Clauser fitting method and the composite profile. Dashed lines represent (1.2) and dash-dotted lines represent (1.3).

## 5.2. Improving accuracy of the indicator function

Another challenge, particularly for single-point experimental hot-wire measurements, is computing wall-normal velocity derivatives and, in particular, the indicator function (5.1). Experimental noise, small measurement errors and sparse wall-normal resolution make it difficult to draw firm conclusions about the existence of a logarithmically scaled region or to identify its start and end points. Similarly, numerical datasets require very high wall-normal resolution to accurately resolve the indicator function, making them computationally expensive at high  $Re_{\tau}$  (Nagib *et al.* 2024).

In contrast, the composite profile provides an analytical representation of the mean velocity profile that can be differentiated analytically, yielding a smooth expression for the indicator function. For example, in the overlap region, the indicator function can be written as

$$z^+ \frac{dU^+}{dz^+} = \frac{\gamma z^+}{\kappa} \cdot \frac{0.6 \xi^5 Re_{\tau} (1 + \eta_{\text{eff}}^6) - \eta_{\text{eff}}^5 z_c^+ (1 + \xi^6)}{z_c^+ Re_{\tau} (1 + \xi^6) (1 + \eta_{\text{eff}}^6)}; \quad \xi = \frac{0.6 z^+}{z_c^+}, \quad \gamma = \sqrt{1 + p_x^+ z_c^+} \quad (5.1)$$

In the high- $Re_\tau$  limit, this expression reduces to  $z^+ \frac{dU^+}{dz^+} = 1/\kappa$ , consistent with the classical log-law behaviour expected in the overlap region of high- $Re_\tau$  TBLs.

The indicator function also provides a useful criterion for assessing the quality of the composite-profile fit. Figure 13(a) compares the indicator function computed directly from the well-resolved ZPG LES of Eitel-Amor *et al.* (2014) with that obtained from the corresponding composite profile, demonstrating excellent agreement.

Further insight can be obtained by considering indicator functions derived from fitted high- $Re_\tau$  experimental datasets. For example, the plateau associated with the overlap region becomes increasingly pronounced as  $Re_\tau$  increases, reflecting the growing separation between the inner and wake regions and therefore a larger overlap-region extent. This behaviour is shown in figure 13(b) for the high- $Re_\tau$  ZPG experimental dataset of Marusic *et al.* (2015). For the highest- $Re_\tau$  case (M8), the pronounced plateau corresponding to  $1/\kappa$  indicates a clear overlap region following classical logarithmic scaling. In contrast, at lower  $Re_\tau$  (e.g. case M1 in figure 13b and the cases in figure 13a), a well-defined plateau is not observed.

The effect of increasing APG on the indicator function at approximately  $Re_\tau = 10,000$  is illustrated in figure 13(c) using experimental datasets from Part 1 with  $\beta_{\text{eff}} = 0, 0.66$  and  $1.44$ . For moderate APGs at high  $Re_\tau$ , the indicator function still exhibits a clear plateau, indicating that the overlap region follows logarithmic scaling. However, as  $\beta_{\text{eff}}$  increases, the wake strengthens and the plateau terminates earlier, reducing the logarithmic extent of the overlap region. Increasing  $\beta_{\text{eff}}$  also reduces the near-wall velocity gradient, decreasing the first peak of the indicator function, while simultaneously increasing the buffer-region overshoot, which deepens the local minimum (figure 13c).

Figure 13(d) further illustrates the influence of PG history on the indicator function and the extent of the overlap region. The case corresponding to  $C_{H_i} = 0.57$  exhibits a slightly longer overlap region than the case with  $C_{H_i} = 1$ , despite having matched  $Re_\tau$  and  $\beta$ .

The composite profile and the associated indicator function can also be used to estimate the number of decades of  $z^+$  over which logarithmic scaling occurs in the overlap region by measuring the plateau extent within a given tolerance (e.g.  $1/\kappa \pm 1\%$ ). Predicted variations in the number of decades of log-law are shown as a function of  $\beta_{\text{eff}}$  and  $Re_\tau$  in figure 14(a). In this analysis the approximations of Perry *et al.* (2002) were employed:  $\Pi = 0.68(\beta + 0.5)^{0.75}$  and  $\delta/\delta^+ = 7.912/(1 + 0.1861\beta)$ , which are valid for  $\beta < 6$ . The results demonstrate competing but expected trends: the logarithmic extent decreases with increasing  $\beta$  at fixed  $Re_\tau$ , but increases with  $Re_\tau$  at fixed  $\beta$ . The red dashed line denotes a minimum 1/3 of a decade in  $z^+$ , roughly corresponding to the predicted logarithmic extent of a ZPG TBL at  $Re_\tau = 3000$ . Such predictions provide useful guidelines for selecting experimental parameter ranges for future investigations of logarithmic scaling in APG TBLs.

The composite profile also predicts the slope of the mean velocity profile in the overlap region, i.e. the von Kármán coefficient. According to (3.6),  $\kappa$  varies as  $\kappa/0.39 = 1/\sqrt{1 + p_x^+ z_c^+}$ . Predicted variations of  $\kappa$  with  $\beta_{\text{eff}}$  are shown as a function of  $Re_\tau$  in figure 14(b). At low  $Re_\tau$ ,  $\kappa$  varies significantly with  $\beta_{\text{eff}}$ , whereas for  $Re_\tau \gtrsim 10,000$  the curves approach  $\kappa = 0.39$  (within typical experimental uncertainty) regardless of  $\beta_{\text{eff}}$ . This indicates that the  $p_x^+$  terms in (3.5) and (3.6) become negligible at sufficiently high  $Re_\tau$ , consistent with (3.8). It also suggests that the hierarchy of attached eddies in the overlap region remains largely unchanged at high  $Re_\tau$ , even under moderate APGs or PG history effects, consistent with Woodcock & Marusic (2015).

Figure 15 shows the estimated wall-normal extent of the log-law, in decades of  $z^+$ , for the datasets in table 1, based on indicator functions derived from the fitted composite profiles. The red dashed line again denotes the approximate threshold of 1/3 of a decade in  $z^+$  required

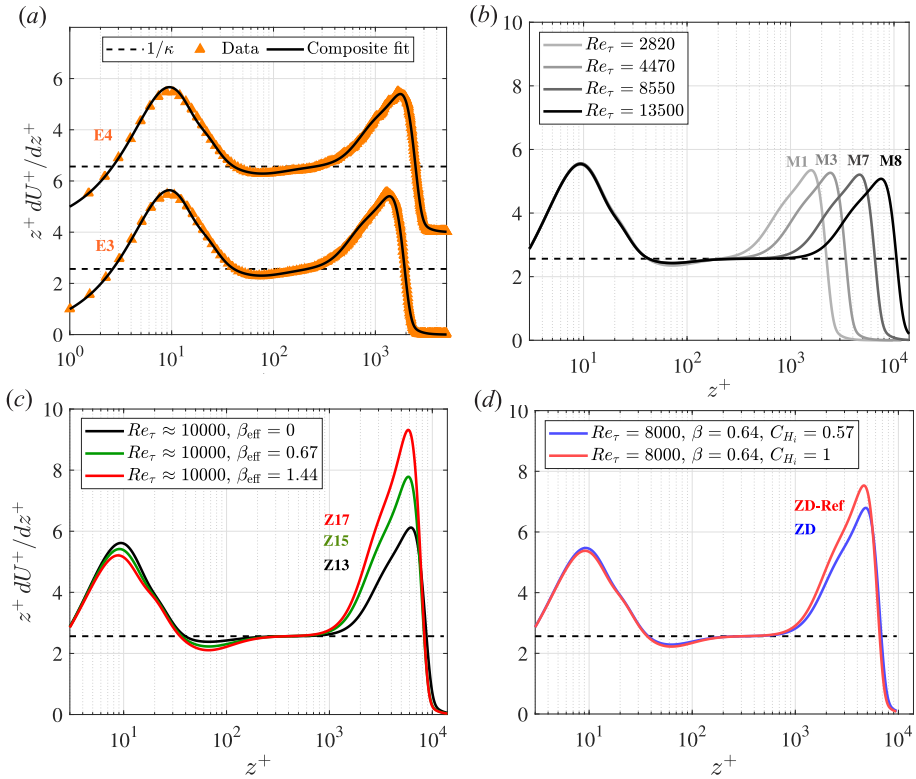


Figure 13: Indicator functions computed from composite profiles fitted to (a) the low- $Re_\tau$  ZPG LES dataset of Eitel-Amor *et al.* (2014), (b) the high- $Re_\tau$  ZPG experimental dataset of Marusic *et al.* (2015), and the high- $Re_\tau$  moderate-APG experimental dataset from Part 1 with (c) minimal PG histories or (d) imposed PG history effects. Horizontal dashed lines represent  $1/\kappa$ .

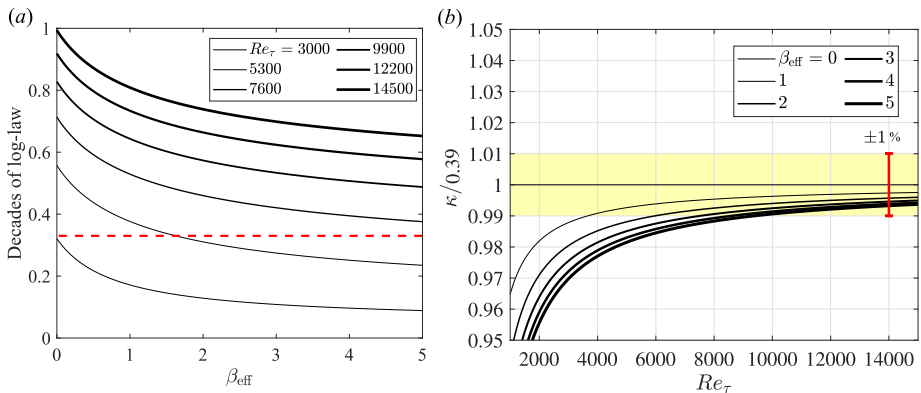


Figure 14: Variation in (a) the decades of  $z^+$  which follow the classical log-law and (b) the value of  $\kappa$  as a function of  $Re_\tau$  and  $\beta_{\text{eff}}$ . The red dashed line indicates 0.33 decades of log-law.

to clearly identify logarithmic scaling. Cases below this threshold are highlighted in yellow, datasets with previously noted PG history effects in the overlap region are highlighted in green, and cases satisfying both conditions are highlighted in red. This comparison highlights the uniqueness of the dataset presented in Part 1, which simultaneously maintains a significant

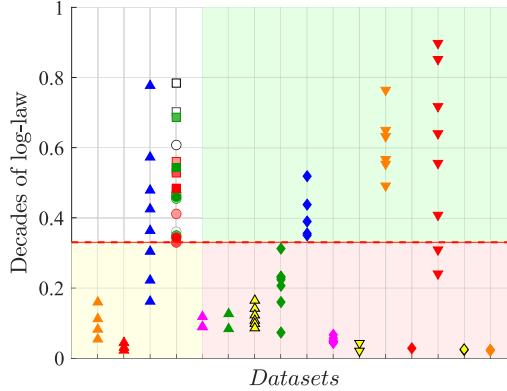


Figure 15: Decades of log-law for the datasets listed in table 1. The red dashed line indicates the threshold of 0.33 decades of log-law. Cases below this threshold are highlighted in yellow, datasets with noted PG history effects in the overlap region are highlighted in green and cases with both conditions are highlighted in red.

overlap region (high  $Re_\tau$  and moderate  $\beta$ ) and controlled PG history effects, enabling a clear investigation of logarithmic scaling in APG TBLs.

A further utility of the composite profile is that it provides an analytical expression from which inflection points ( $d^2U/dz^2 = 0$ ) can be identified. This is useful for testing the framework of Schatzman & Thomas (2017), which links APG-induced energisation of wake-region motions to a shear instability associated with an inflectional mean velocity profile. The availability of an analytical composite profile, therefore, facilitates identification of these inflection points and further assessment of this mechanism for APG TBL dynamics.

## 6. Conclusions

This study presents a novel and practical composite profile formulation, (3.5)–(3.7), for the mean streamwise velocity in adverse-pressure-gradient (APG) turbulent boundary layers (TBLs), with three physically meaningful free parameters:  $z_c^+$ ,  $C_{H_w}$  and  $\Pi$ . The formulation is motivated by the results of Part 1 and strategically modifies the earlier composite profile of Nickels (2004), originally developed for generic low- $Re_\tau$  pressure-gradient TBLs, with the aim of extending its applicability to a broader range of Reynolds numbers and PG conditions.

Several key modifications were introduced. First, the wake function was reformulated to be consistent with an independent and physically motivated definition of the boundary-layer thickness (Lozier *et al.* 2025), together with the introduction of a wake-history parameter  $C_{H_w}$  that accounts for pressure-gradient history effects in the wake region. Second, a velocity-overshoot function was incorporated in the inner region, consistent with the approaches of Monkewitz *et al.* (2007) and Chauhan *et al.* (2009). Third, the relationship between streamwise PGs and the sublayer thickness  $z_c^+$  originally proposed by Nickels (2004) was reformulated through (3.3) in light of recent high- $Re_\tau$  APG TBL studies.

The proposed composite profile was evaluated using a compilation of APG TBL datasets spanning more than three decades of experimental and numerical investigations, with particular emphasis on the high- $Re_\tau$  dataset presented in Part 1. A nonlinear least-squares curve-fitting procedure, implemented in the accompanying [notebooks](#), was used to optimise the free parameters and fit the mean velocity profiles across all cases considered. The resulting fits demonstrate that the composite profile provides an accurate representation of the mean

velocity structure across a wide range of Reynolds numbers, pressure-gradient magnitudes and PG-history conditions.

The optimised parameters further enable the development of a framework for interpreting PG-history effects. In particular, the wake-history parameter  $C_{H_w}$  quantifies the influence of upstream PG development on the wake-region structure, while the effective pressure-gradient parameter  $\beta_{\text{eff}}$  (or equivalently  $C_{H_i}$ ), derived from  $z_c^+$ , characterises the combined influence of local and upstream PGs on the overlap-region velocity shift. These parameters provide a practical criterion for identifying ‘well-behaved’ APG TBLs, for which  $C_{H_w} \approx 1$  and  $\beta = \beta_{\text{eff}}$ , and allow cases with PG history to be classified in terms of ‘history-enhanced’ or ‘history-damped’ modifications to the mean velocity profile.

The composite profile also provides several practical utilities for analysing APG TBL datasets. In particular, it enables estimation of the friction velocity  $U_\tau$  and boundary-layer thickness  $\delta$  in cases where these quantities cannot be measured accurately, provided the PG history is minimal or well characterised. For the dataset from Part 1, the values of  $U_\tau$  and  $\delta$  obtained from this approach agree with direct experimental measurements within typical experimental uncertainty. The analytical form of the composite profile additionally allows smooth differentiation of the mean velocity profile, facilitating evaluation of the indicator function and identification of inflection points, which are often difficult to obtain from sparse or noisy experimental data. The formulation also enables predictions regarding the dependence of the logarithmic-region extent and the von Kármán coefficient on Reynolds number and pressure-gradient strength, providing useful guidance for future experimental investigations.

Beyond providing an accurate analytical representation of the mean velocity profile, the formulation also yields several physical insights. The results demonstrate that pressure-gradient history modifies the mean velocity profile in distinct ways across the boundary layer, influencing both the overlap-region velocity shift and the wake-region structure through separate mechanisms characterised by  $C_{H_i}$  and  $C_{H_w}$ . The concept of an effective pressure gradient  $\beta_{\text{eff}}$  provides a simple framework for interpreting the combined influence of local and upstream PGs on overlap scaling.

In summary, the composite profile formulation introduced here provides a unified and physically interpretable description of APG TBL mean velocity profiles across a wide range of Reynold numbers and pressure-gradient conditions. While the formulation is broadly applicable to pressure-gradient TBLs, it has not yet been tested extensively for favourable pressure gradients or flows approaching separation. Additional high-fidelity experimental and numerical datasets, particularly at high Reynolds numbers, will therefore be valuable for further refining the model. Extending the framework to rough-wall TBLs would likely require additional parameters, and further investigations of rough-wall pressure-gradient boundary layers are needed to support such developments.

**Acknowledgements.** The authors gratefully acknowledge funding from the Office of Naval Research (ONR) and ONR Global; Grant No. N62909-23-1-2068. R. Deshpande also acknowledges financial support from the Melbourne Postdoctoral Fellowship awarded by the University of Melbourne.

**Declaration of Interests.** The authors report no conflict of interest.

## Appendix A. Fitting results for all datasets considered in the present study

Dataset	Case no	$\beta$	$Re_\tau$	$p_x^+ \times 10^4$	$\Pi$	$z_c^+$	$C_{H_w}$	$C_{H_i}$	$\beta_{\text{eff}}$	$\delta$
<i>Datasets with all relevant TBL properties known.</i>										
Zarei <i>et al.</i> (2026)	ZA	0	4550	0	0.6	11.74	0.94	1.33	0.27	132.8
	ZA-Ref.	0	4090	0	0.45	12	1	1	0	124

*Continued on next page*

(Continued from previous page)

Dataset	Case no	$\beta$	$Re_{\tau}$	$p_x^+ \times 10^4$	$\Pi$	$z_c^+$	$C_{Hw}$	$C_{Hi}$	$\beta_{eff}$	$\delta$
	ZB	0	5840	0	0.66	12	1	1	0	200
	ZC	0	7440	0	0.79	12	1	1	0	268
	ZD	0.64	8000	6.5	1	11.64	0.96	0.58	0.37	296
	ZD-Ref.	0.65	7850	6.6	1.15	11.36	1	1	0.65	295
	ZE	1.47	9790	9.8	1.51	10.83	1	1	1.46	434
	ZE-Ref.	1.46	10000	10	1.5	10.8	1	1	1.46	440
	Z1	0	6380	0	0.71	12.00	1	1	0	204
	Z2	0	4340	0	0.79	12.00	1	1	0	203
	Z3	0	6610	0	0.6	12.00	1	1	0	207
	Z4	0	4310	0	0.61	12.00	1	1	0	193
	Z5	0	6150	0	0.71	12.00	1	1	0	200
	Z6	0	4390	0	0.68	12.00	1	1	0	195
	Z7	0	8300	0	0.73	12.00	1	1	0	273
	Z8	0	5800	0	0.86	12.00	1	1	0	284
	Z9	0.34	8220	3.6	0.84	11.67	1	1	0.34	284
	Z10	0.34	5650	4.7	1.03	11.67	1	1	0.34	293
	Z11	0.57	8430	5.8	0.98	11.46	1	1	0.57	305
	Z12	0.58	5760	7.5	1.20	11.45	1	1	0.58	311
	Z13	0	10680	0	0.85	12.00	1	1	0	370
	Z14	0	7340	0	0.94	12.00	1	1	0	368
	Z15	0.67	9970	5.1	1.19	11.38	1	1	0.67	387
	Z16	0.66	7000	6.7	1.28	11.39	1	1	0.66	399
	Z17	1.44	9680	9.8	1.50	10.84	1	1	1.44	419
	Z18	1.44	6760	13.2	1.63	10.84	1	1	1.44	421
Li <i>et al.</i> (2021)	L1	0	8610	0	1.47	11.09	1.14	1.08	1.06	154
	L2	0	8880	0	1.24	11.16	1.04	1.08	0.96	156
	L3	0	8920	0	1.00	11.56	0.94	1.04	0.47	159
	L4	0	10880	0	0.71	11.60	0.88	1.03	0.42	182
	L5	0	12430	0	0.65	11.69	0.88	1.03	0.32	216
	L6	0	14650	0	0.61	12.00	0.94	1.00	0.00	244
	L7	0	20770	0	0.57	12.00	1.01	1.00	0.00	345
	L8	0	23930	0	0.56	11.95	1.01	1.00	0.00	418
Eitel-Amor <i>et al.</i> (2014)	E1	0	1200	0	0.63	12.00	1.00	1.00	0.00	66
	E2	0	1960	0	0.70	12.00	1.00	1.00	0.00	114
	E3	0	2460	0	0.71	12.00	1.00	1.00	0.00	147
	E4	0	3140	0	0.71	12.00	1.00	1.00	0.00	191
Örlü & Schlatter (2013)	O1	0	1970	0	0.59	12.00	1.06	1.00	0.00	38
	O2	0	1160	0	0.61	12.00	1.00	1.00	0.00	34
	O3	0	1150	0	0.63	12.00	1.00	1.00	0.00	34
Marusic <i>et al.</i> (2015)	M1	0	2820	0	0.69	12.00	1.00	1.00	0.00	58
	M2	0	3570	0	0.71	12.00	1.00	1.00	0.00	75
	M3	0	4470	0	0.66	12.00	1.00	1.00	0.00	95
	M4	0	5130	0	0.63	12.00	1.00	1.00	0.00	109
	M5	0	6050	0	0.66	12.00	1.00	1.00	0.00	133
	M6	0	6790	0	0.63	12.00	1.00	1.00	0.00	150
	M7	0	8550	0	0.66	12.00	1.00	1.00	0.00	190
	M8	0	13500	0	0.63	12.00	1.00	1.00	0.00	319
(different tripping)	MA	0	6040	0	0.06	12.00	0.85	1.00	0.00	119
	MB	0	8840	0	0.32	12.00	1.13	1.00	0.00	187
	MC	0	10280	0	0.44	12.00	1.14	1.00	0.00	225
	MD	0	11940	0	0.55	12.00	1.00	1.00	0.00	271
Monty <i>et al.</i> (2011)	T1	0	2970	0	0.65	12.00	1.08	1.00	0.00	62
	T2	1.52	3170	34.1	1.26	10.79	1.14	1.00	1.52	90
Volino (2020)	VA	0.00	1060	0.0	0.74	11.88	0.88	1.01	0.12	14
	VB	0.00	1450	0.0	0.74	12.10	1.28	0.99	-0.09	20
	V1	2.65	1130	118.5	1.31	11.61	0.94	0.15	0.41	18
	V2	4.09	1150	158.2	1.82	11.64	0.94	0.09	0.37	21
	V3	6.60	1150	222.8	2.53	11.40	0.92	0.10	0.65	25
	V4	0.79	1360	36.6	1.37	11.98	1.20	0.02	0.02	22
	V5	0.92	1190	38.6	1.94	12.00	1.08	0.00	0.00	24
	V6	1.02	1100	36.4	2.66	12.00	0.95	0.00	0.00	25
Sanmiguel Vila <i>et al.</i> (2020)	SA	0.00	1430	-0.2	0.68	12.27	1.09	0.98	-0.25	18
	SB	0.04	2020	1.7	0.86	12.66	1.14	0.95	-0.56	27
	S1	0.38	3140	9.5	1.06	12.99	1.13	-2.05	-0.78	48

Continued on next page

(Continued from previous page)

Dataset	Case no	$\beta$	$Re_\tau$	$p_x^+ \times 10^4$	$\Pi$	$z_c^+$	$C_{H_w}$	$C_{H_i}$	$\beta_{\text{eff}}$	$\delta$
	S2	0.69	3310	14.9	1.17	13.03	1.06	-1.16	-0.80	54
	S3	1.23	3660	21.8	1.37	12.54	1.05	-0.38	-0.46	65
	S4	1.94	4200	27.5	1.59	12.25	1.02	-0.12	-0.23	81
	S5	1.97	4980	20.9	2.04	11.96	1.02	0.02	0.04	115
	S6	2.17	4650	25.7	1.93	12.21	1.03	-0.09	-0.19	101
	S7	2.19	5070	22.3	2.01	12.13	0.98	-0.06	-0.12	117
Bobke <i>et al.</i> (2017)	B1	1.03	580	83.9	1.39	10.75	0.94	1.54	1.58	45.9
	B2	1.64	900	80.9	1.96	10.32	0.91	1.43	2.36	97.8
Pozuelo <i>et al.</i> (2022)	P1	1.03	600	91.2	1.14	10.9	0.99	1.31	1.34	41.9
	P2	1.65	920	84.7	1.73	10.84	0.95	0.87	1.43	88.9
<i>Datasets where <math>\delta</math> is not known.</i>										
Nagano <i>et al.</i> (1998)	N1	0.77	420	91.2	0.83	11.33	0.96	1.00	0.77	16
	N2	3.95	570	256.0	2.14	9.64	0.93	1.00	3.95	34
	N3	5.32	600	287.0	2.99	9.18	0.92	1.00	5.32	46
Preskett <i>et al.</i> (2025)	K1	0.00	6840	0.0	0.29	12.44	1.13	0.96	-0.38	93
	K2	0.00	7290	0.0	0.48	12.19	1.03	0.98	-0.18	104
	K3	0.00	7520	0.0	0.69	12.43	1.01	0.97	-0.38	113
	K4	0.00	7890	0.0	1.04	12.56	0.91	0.96	-0.48	125
	K5	0.00	8330	0.0	1.21	12.11	0.91	0.99	-0.11	135
	K6	0.00	9440	0.0	1.80	11.95	0.84	1.00	0.05	159
Romero <i>et al.</i> (2022)	R1	0.90	7100	10.7	0.64	10.81	0.78	1.64	1.48	417
	R2	1.11	7120	12.3	0.69	10.12	0.67	2.50	2.77	434
	R3	1.65	7130	18.5	0.93	12.16	0.81	-0.09	-0.15	464
	R4	1.70	7640	18.3	1.01	11.46	0.67	0.34	0.58	528
	R5	1.77	7770	17.1	1.11	11.26	0.74	0.47	0.84	567
Yoon <i>et al.</i> (2018)	Y1	1.45	834	10.0	1.63	11.35	0.99	0.49	0.71	44
Gungor <i>et al.</i> (2024)	G1	0.22	860	15.9	0.63	11.88	1.01	0.55	0.12	6
	G2	0.01	1520	28.4	5.54	8.47	0.98	1.42	8.21	33
<i>Dataset where <math>\delta</math> and <math>U_\tau</math> are not known.</i>										
Marusic & Perry (1995)	A1	0.00	2840	0.0	0.53	12.00	1.00	1.00	0.00	39
	A2	0.68	3210	10.0	0.76	11.38	1.00	1.00	0.68	48
	A3	1.28	3590	20.0	1.03	10.94	1.00	1.00	1.28	61
	A4	2.42	3930	30.0	1.44	10.29	1.00	1.00	2.42	76
	A5	3.38	4110	40.0	1.78	9.86	1.00	1.00	3.38	88
	A6	4.99	4170	50.0	2.24	9.28	1.00	1.00	4.99	99

Table 2: Complete list of datasets/cases considered here with corresponding fitting results (see [notebooks](#)). Inputs and outputs of the composite profile fitting method, as described in section 3, are highlighted in yellow and green, respectively.

## Appendix B. Overshoot function

The maximum overshoot from the log-law in the buffer region, i.e.  $f(z_c^+)$  from (3.2), was measured for all cases in the present study, and the results are plotted as a function of  $\beta_{\text{eff}}$  (3.3) in figure 16. A clear trend is observed: the overshoot increases with  $\beta_{\text{eff}}$  for the range of APG TBLs considered here; however, the overshoot can not grow unboundedly. As such, we propose the following functional form for the maximum overshoot from the log-law as a function of  $z_c^+$ , or equivalently  $\beta_{\text{eff}}$ :

$$f(z_c^+) = 0.23 + 0.5 \tanh\left(31 \frac{144 - z_c^{+2}}{z_c^{+3}}\right) = 0.23 + 0.5 \tanh(0.45\beta_{\text{eff}}). \quad (\text{B } 1)$$

From figure 16, a clear agreement between this model and the measured overshoots can be observed, with all cases matching within experimental uncertainty. Consequently, with the overshoot well-modelled, the proposed composite profile (3.5) can remain a three-parameter composite profile. It is also noted that this proposed model (B 1) has a formulation consistent

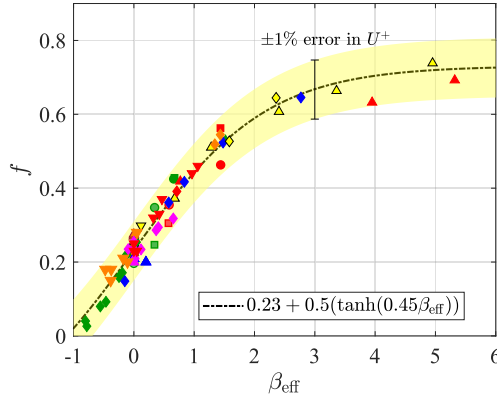


Figure 16: Maximum overshoot of the mean velocity in the buffer region as a function of  $\beta_{\text{eff}}$ .

with previous studies/datasets, such as Chauhan *et al.* (2009) and Monkewitz (2021); however, further high- $Re_\tau$  studies across a broader range of  $\beta_{\text{eff}}$  are necessary to refine this formulation. The underlying mechanism behind the apparent increase in  $f(z_c^+)$  under an APG can also be analysed through the mean momentum balance (MMB) equation for TBLs (Klewicki 2013). The MMB equation includes contributions from the mean inertia (MI), pressure gradient (PG), turbulent inertia (TI), and viscous force (VF) terms. In the buffer region, the MI term is negligible and, in the absence of any PG, the VF and TI terms are balanced, i.e.  $\partial(VF)/\partial(TI) \approx 1$ . However, by introducing an APG ( $dp/dx < 0$ ), this balance shifts, reducing the relative contribution of viscous forces  $\partial(VF)/\partial(TI) < 1$  (See figures 1 and 3 from Romero *et al.* 2022, and figures 14 and 15 from Han *et al.* 2024). The hypothesis is that this interplay between decreasing viscous and increasing turbulent stresses leads to an imbalance, meaning that Reynolds stress builds up more rapidly than viscous stress can dissipate it, causing the mean velocity profile to overshoot before settling back to the log-law.

### Appendix C. Identifying other upstream history effects

Changes in tripping conditions and/or perturbations in the surface condition/roughness, also leave ‘history’ effects on the TBL mean velocity profile, irrespective of PG history effects, primarily affecting large-scale structures and reshaping the wake region (Marusic *et al.* 2015; Örlü *et al.* 2010). Interestingly, we can identify these other history effects using the same composite profile, which can further contribute to the characterisation of ‘well-behaved’ TBLs ( $C_{H_i} \approx C_{H_w} \approx 1$ ). Here, we consider datasets from Marusic *et al.* (2015) and Örlü *et al.* (2010), which employ various tripping conditions, as well as the dataset from Li *et al.* (2021), which involves a sudden change in surface condition from rough to smooth. The calculated values of  $C_{H_w}$  and  $C_{H_i}$ , along with examples of the corresponding composite profiles, are shown in figure 17. As shown, once the TBL has recovered ZPG-like statistics, consistent with the observations reported in the cited studies, both  $C_{H_w}$  and  $C_{H_i}$  also converge toward unity. In addition, while tripping conditions primarily affect the wake region (changing  $C_{H_w}$ ), it typically leaves the inner/overlap region ( $C_{H_i}$ ) unaffected, as seen in figure 17. In contrast, for the case with the rough to smooth transition,  $C_{H_w}$  and  $C_{H_i}$  both change *independently*, and a fundamentally different physical framework must be considered to interpret these changes, e.g. a ‘blending model’ for the mean velocity profile (Li *et al.* 2021) where a smooth-wall profile approximates the flow near the wall while the wake region retains rough-wall characteristics.

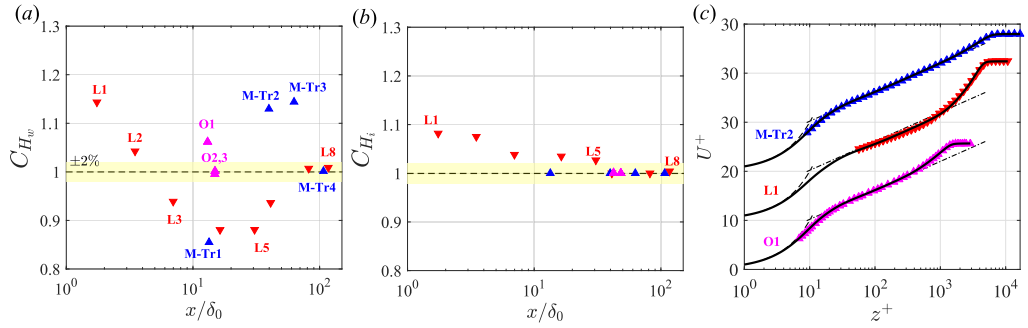


Figure 17: Variations in (a)  $C_{H_w}$  and (b)  $C_{H_i}$ , and (c) example mean velocity profiles with their corresponding fitted composite profiles for cases with minimal PG history effects but different tripping/surface roughness histories. The shaded yellow region indicates  $\pm 2\%$  error.

## REFERENCES

- BOBKE, A., VINUESA, R., ÖRLÜ, R. & SCHLATTER, P. 2017 History effects and near equilibrium in adverse-pressure-gradient turbulent boundary layers. *J. Fluid Mech.* **820**, 667–692.
- CANTWELL, B. J., BILGIN, E. & NEEDELS, J. T. 2022 A new boundary layer integral method based on the universal velocity profile. *Phys. Fluids* **34** (7).
- CHAUHAN, K., NAGIB, H. & MONKEWITZ, P. 2007 On the composite logarithmic profile in zero pressure gradient turbulent boundary layers. In *45th AIAA Aerospace Sciences Meeting and Exhibit*, p. 532.
- CHAUHAN, K. A., MONKEWITZ, P. A. & NAGIB, H. M. 2009 Criteria for assessing experiments in zero pressure gradient boundary layers. *Fluid Dyn. Res.* **41** (2), 021404.
- CLAUSER, F. H. 1954 Turbulent boundary layers in adverse pressure gradients. *J. Aeronaut. Sci.* **21** (2), 91–108.
- CLAUSER, F. H. 1956 The turbulent boundary layer. *Adv. Appl. Mech.* **4**, 1–51.
- COLES, D. 1956 The law of the wake in the turbulent boundary layer. *J. Fluid Mech.* **1** (2), 191–226.
- DESHPANDE, R., VAN DEN BOGAARD, A., VINUESA, R., LINDIĆ, L. & MARUSIC, I. 2023 Reynolds-number effects on the outer region of adverse-pressure-gradient turbulent boundary layers. *Phys. Rev. Fluids* **8** (12), 124604.
- DRÓZDZ, A., ELSNER, W., NIEGODAJEW, P., VINUESA, R., ÖRLÜ, R. & SCHLATTER, P. 2020 A description of turbulence intensity profiles for boundary layers with adverse pressure gradient. *Eur. J. Mech. B Fluids* **84**, 470–477.
- EITEL-AMOR, G., ÖRLÜ, R. & SCHLATTER, P. 2014 Simulation and validation of a spatially evolving turbulent boundary layer up to  $Re_\theta = 8300$ . *Int. J. Heat Fluid Flow* **47**, 57–69.
- GUNGOR, T. R., GUNGOR, A. G. & MACIEL, Y. 2024 Turbulent boundary layer response to uniform changes of the pressure force contribution. *J. Fluid Mech.* **997**, A75.
- HAN, M., MA, M. & YAN, C. 2024 Consistent outer scaling and analysis of adverse pressure gradient turbulent boundary layers. *J. Fluid Mech.* **982**, A17.
- HARUN, Z., MONTY, J. P., MATHIS, R. & MARUSIC, I. 2013 Pressure gradient effects on the large-scale structure of turbulent boundary layers. *J. Fluid Mech.* **715**, 477–498.
- JONES, M. B., MARUSIC, I. & PERRY, A. E. 2001 Evolution and structure of sink-flow turbulent boundary layers. *J. Fluid Mech.* **428**, 1–27.
- KLEWICKI, J. C. 2013 A description of turbulent wall-flow vorticity consistent with mean dynamics. *J. Fluid Mech.* **737**, 176–204.
- KRUG, D., PHILIP, J. & MARUSIC, I. 2017 Revisiting the law of the wake in wall turbulence. *J. Fluid Mech.* **811**, 421–435.
- LI, M., DE SILVA, C. M., CHUNG, D., PULLIN, D. I., MARUSIC, I. & HUTCHINS, N. 2021 Experimental study of a turbulent boundary layer with a rough-to-smooth change in surface conditions at high Reynolds numbers. *J. Fluid Mech.* **923**, A18.
- LONG, R. R. & CHEN, T-C. 1981 Experimental evidence for the existence of the ‘mesolayer’ in turbulent systems. *J. Fluid Mech.* **105**, 19–59.
- LOZIER, M., DESHPANDE, R., ZAREI, A., LINDIĆ, L., ROWIN, W. A. & MARUSIC, I. 2025 Defining the mean

- turbulent boundary layer thickness based on streamwise velocity skewness. *J. Fluid Mech.* **1021**, A19.
- MARUSIC, I., CHAUHAN, K. A., KULANDAIVELU, V. & HUTCHINS, N. 2015 Evolution of zero-pressure-gradient boundary layers from different tripping conditions. *J. Fluid Mech.* **783**, 379–411.
- MARUSIC, I., MCKEON, B. J., MONKEWITZ, P. A., NAGIB, H. M., SMITS, A. J. & SREENIVASAN, K. R. 2010 Wall-bounded turbulent flows at high Reynolds numbers: recent advances and key issues. *Phys. Fluids* **22** (6).
- MARUSIC, I., MONTY, J. P., HULTMARK, M. & SMITS, A. J. 2013 On the logarithmic region in wall turbulence. *J. Fluid Mech.* **716**, R3.
- MARUSIC, I. & PERRY, A. E. 1995 A wall-wake model for the turbulence structure of boundary layers. Part 2. further experimental support. *J. Fluid Mech.* **298**, 389–407.
- MILLIKAN, C. 1938 A critical discussion of turbulent flows in channels and circular tubes. In *Proc. 5th Int. Cong. Appl. Mech.*, pp. 386–392.
- MONKEWITZ, P. A. 2021 The late start of the mean velocity overlap log law at—a generic feature of turbulent wall layers in ducts. *J. Fluid Mech.* **910**, A45.
- MONKEWITZ, P. A., CHAUHAN, K. A. & NAGIB, H. M. 2007 Self-consistent high-Reynolds-number asymptotics for zero-pressure-gradient turbulent boundary layers. *Phys. Fluids* **19** (11).
- MONKEWITZ, P. A. & NAGIB, H. M. 2023 The hunt for the Kármán ‘constant’ revisited. *J. Fluid Mech.* **967**, A15.
- MONTY, J. P., HARUN, Z. & MARUSIC, I. 2011 A parametric study of adverse pressure gradient turbulent boundary layers. *Int. J. Heat Fluid Flow* **32** (3), 575–585.
- MUSKER, A. J. 1979 Explicit expression for the smooth wall velocity distribution in a turbulent boundary layer. *AIAA J.* **17** (6), 655–657.
- NAGANO, Y., TSUJI, T. & HOURA, T. 1998 Structure of turbulent boundary layer subjected to adverse pressure gradient. *Int. J. Heat Fluid Flow* **19** (5), 563–572.
- NAGIB, H., VINUESA, R. & HOYAS, S. 2024 Utilizing indicator functions with computational data to confirm nature of overlap in normal turbulent stresses: Logarithmic or quarter-power. *Phys. Fluids* **36** (7).
- NICKELS, T. B. 2004 Inner scaling for wall-bounded flows subject to large pressure gradients. *J. Fluid Mech.* **521**, 217–239.
- ÖRLÜ, R., FRANSSON, J. H. M. & ALFREDSSON, P. H. 2010 On near wall measurements of wall bounded flows—the necessity of an accurate determination of the wall position. *Prog. Aerosp. Sci.* **46** (8), 353–387.
- ÖRLÜ, R. & SCHLATTER, P. 2013 Comparison of experiments and simulations for zero pressure gradient turbulent boundary layers at moderate Reynolds numbers. *Exp. Fluids* **54**, 1–21.
- PANTON, R. L. 2005 Review of wall turbulence as described by composite expansions. *App. Mech. Rev.* **58**, 1–36.
- PERRY, A. E., MARUSIC, I. & JONES, M. B. 2002 On the streamwise evolution of turbulent boundary layers in arbitrary pressure gradients. *J. Fluid Mech.* **461**, 61–91.
- POZUELO, R., LI, Q., SCHLATTER, P. & VINUESA, R. 2022 An adverse-pressure-gradient turbulent boundary layer with nearly constant  $\beta \approx 1.4$  up to  $Re_\theta \approx 8700$ . *J. Fluid Mech.* **939**, A34.
- PRESKETT, T., VIRGILIO, M., JAISWAL, P. & GANAPATHISUBRAMANI, B. 2025 Effects of pressure-gradient histories on skin friction and mean flow of high Reynolds number turbulent boundary layers over smooth and rough walls. *J. Fluid Mech.* **1010**, A30.
- ROMERO, S., ZIMMERMAN, S., PHILIP, J. & KLEWICKI, J. 2023 Velocity spectra and scale decomposition of adverse pressure gradient turbulent boundary layers considering history effects. *Int. J. Heat Fluid Flow* **102**, 109143.
- ROMERO, S., ZIMMERMAN, S., PHILIP, J., WHITE, C. & KLEWICKI, J. 2022 Properties of the inertial sublayer in adverse pressure-gradient turbulent boundary layers. *J. Fluid Mech.* **937**, A30.
- SANMIGUEL VILA, C., VINUESA, R., DISCETTI, S., IANIRO, A., SCHLATTER, P. & ÖRLÜ, R. 2017 On the identification of well-behaved turbulent boundary layers. *J. Fluid Mech.* **822**, 109–138.
- SANMIGUEL VILA, C., VINUESA, R., DISCETTI, S., IANIRO, A., SCHLATTER, P. & ÖRLÜ, R. 2020 Experimental realisation of near-equilibrium adverse-pressure-gradient turbulent boundary layers. *Exp. Therm. Fluid Sci.* **112**, 109975.
- SCHATZMAN, D. M. & THOMAS, F. O. 2017 An experimental investigation of an unsteady adverse pressure gradient turbulent boundary layer: embedded shear layer scaling. *J. Fluid Mech.* **815**, 592–642.
- SHARMA, A. S. & MCKEON, B. J. 2013 On coherent structure in wall turbulence. *J. Fluid Mech.* **728**, 196–238.

- SHU, Z. & XU, C. 2025 Mean velocity profiles and total shear stress profiles in adverse-pressure-gradient turbulent boundary layers considering history effect. *arXiv preprint arXiv:2508.07663* .
- SPALDING, D. B. 1961 A single formula for the law of the wall. *J. Appl. Mech.* **28** (3), 455–458.
- SUBRAHMANYAM, M. A., CANTWELL, B. J. & ALONSO, J. J. 2022 A universal velocity profile for turbulent wall flows including adverse pressure gradient boundary layers. *J. Fluid Mech.* **933**, A16.
- VAN DRIEST, E. R. 1956 On turbulent flow near a wall. *J. Aeronaut. Sci.* **23** (11), 1007–1011.
- VAN DRIEST, E. R. & BLUMER, C. B. 1963 Boundary layer transition-freestream turbulence and pressure gradient effects. *AIAA J.* **1** (6), 1303–1306.
- VINUESA, R., ÖRLÜ, R., SANMIGUEL VILA, C., IANIRO, A., DISCETTI, S. & SCHLATTER, P. 2017 Revisiting history effects in adverse-pressure-gradient turbulent boundary layers. *Flow Turbul. Combust.* **99**, 565–587.
- VOLINO, R. J. 2020 Non-equilibrium development in turbulent boundary layers with changing pressure gradients. *J. Fluid Mech.* **897**, A2.
- WOODCOCK, J. D. & MARUSIC, I. 2015 The statistical behaviour of attached eddies. *Phys. Fluids* **27** (1).
- YANG, X. I. A., CHEN, P. E. S., ZHANG, W. & KUNZ, R. 2024 Predictive near-wall modelling for turbulent boundary layers with arbitrary pressure gradients. *J. Fluid Mech.* **993**, A1.
- YOON, M., HWANG, J. & SUNG, H. J. 2018 Contribution of large-scale motions to the skin friction in a moderate adverse pressure gradient turbulent boundary layer. *J. Fluid Mech.* **848**, 288–311.
- ZAREI, A., LOZIER, M., DESHPANDE, R. & MARUSIC, I. 2026 High-Reynolds-number turbulent boundary layers under adverse pressure gradients. Part 1. Decoupling pressure gradient history effects. *J. Fluid Mech.* Under review, arXiv preprint arXiv:2509.07545.